ACS OMEGA
http://pubs.acs.org/journal/acsodf
Article

Open Access
This article is licensed under CC-BY-NC-ND 4.0

Downloaded via UNIV DE ZARAGOZA on January 15, 2025 at 13:10:50 (UTC).
See https://pubs.acs.org/sharingguidelines for options on how to legitimately share published articles.

Tailoring Nickel Oxide Thin Films: Comparative Study of Oxidizing Agents in Thermal and Plasma-Enhanced Atomic Layer Deposition

Mario Alberto Hidrogo-Rico, Nicola Nedev, Paul Horley, María Isabel Mendívil, Jhonathan Castillo-Saenz, Edgar Martínez-Guerra, Emilio J. Juarez-Perez, Francisco Servando Aguirre-Tostado, Arturo Susarrey-Arce, and Eduardo Martínez-Guerra*

Cite This: *ACS Omega* 2025, 10, 422−438
Read Online

ACCESS | Metrics & More | Article Recommendations | Supporting Information

ABSTRACT: Thermal atomic layer deposition (TALD) and plasma atomic layer deposition (PALD) were used for producing thin NiO_x films from nickel(II) acetylacetonate $Ni(acac)_2$, employing different oxidizing agents (deionized water H_2O, ozone O_3, and molecular oxygen O_2). The films were deposited at 300 °C (TALD) and 220 °C (PALD) over glass substrates; their physical and chemical properties were considerably influenced by the choice of oxidizing agents. In particular, ALD(H_2O) samples had a low growth per cycle (GPC) and a high concentration of defects. The best NiO_x parameters were achieved with PALD(O_2), featuring high GPC (0.07 nm/cycle), high optical transparency in the visible region, electrical resistivity (1.18×10^4 Ω·cm), good carrier concentration (8.82×10^{13} cm^{-3}), and common mobility (5.98 $cm^2/V \cdot s$). The resulting NiO_x films are polycrystalline and homogeneous in thickness and composition. According to ultraviolet photoelectron spectroscopy (UPS), work function φ and the valence band maximum E_V can be tuned by the choice of the coreactant employed, with variations of up to ∼1 eV between TALD and PALD synthesis. Our results suggest that PALD permits one to achieve a better energy band alignment of NiO_x and CsFAMAPbBrI perovskite, which is promising for solar cell applications.

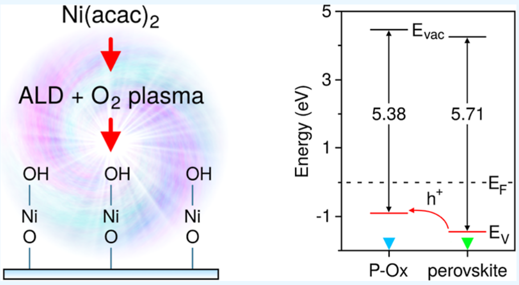

1. INTRODUCTION

Nickel oxide (NiO_x) with a rock salt structure has attracted considerable scientific attention due to its low toxicity and remarkable stability under ambient conditions. This II−VI material has a wide direct band gap (3.4−4.3 eV) with a deep valence band edge (∼5.4 eV) providing high optical transparency. The work function of NiO_x can be controllably adjusted in a wide energy range (3.7−6.7 eV) by fine-tuning defect density and material composition. The principal physical properties of nickel oxide—optical,[1] electrical,[2] magnetic,[3] and thermal[4]—are defined by its stoichiometry; they vary with nickel oxidation state and Ni/O ratio, which also establishes the presence of cation vacations.[5] By modifying the Ni/O ratio, this material can be converted into nickel oxide, an intrinsic p-type semiconductor with a relatively low electron affinity of 1.8 eV.[6] Stoichiometric nickel oxide is an antiferromagnetic insulator with resistivity of up to 10^{13} Ω·cm.[7] Thin NiO_x films are promising for several microelectronic applications that are defined by material stoichiometry. Its principal uses include antiferromagnetic layers,[8] p-type transparent conducting films,[9] active elements of electrochromic devices,[10,11] functional layers of chemical sensors,[12] and inorganic hole transport layers for perovskite solar cells.[13] The best-quality NiO_x films are produced with a carefully controlled conformal growth process.

NiO_x can be synthesized using physical and chemical routes[14] such as pulsed laser deposition,[15] sputtering,[16] thermal evaporation,[17] sol−gel technique,[18,19] chemical bath deposition,[20] spray pyrolysis,[21] and atomic layer deposition (ALD).[22−26] The latter method permits an extraordinary control of the entire deposition process at the subnanometer scale, resulting in excellent surface coverage degree.[27] ALD as a chemical method is governed by a complex sequence of reactions. Uniform coating can be produced over large areas under relatively low temperatures, which is ideal for obtaining high-quality, pinhole-free conformal thin films.[28] The fine control and reproducibility characteristics of ALD allow the remarkably simple tailoring of chemical, optical, and electronic properties of the resulting films, producing consistent stoichiometry, material density, and a uniform intentional doping with the desired impurity concentration.[29,30] The ALD process involves two chemical reactions between gas-phase reagents and the film surface, which rely heavily on reactivity and stability of the reactants.[25] In plasma-enhanced ALD

Received: July 17, 2024
Revised: November 22, 2024
Accepted: December 18, 2024
Published: December 30, 2024

ACS Publications

© 2024 The Authors. Published by American Chemical Society

https://doi.org/10.1021/acsomega.4c06606
ACS Omega 2025, 10, 422−438

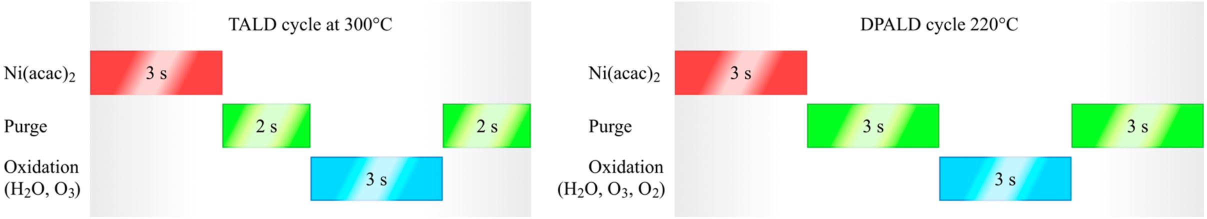

Figure 1. Schematic diagrams of TALD and PALD cycles used for deposition of NiO_x.

[plasma atomic layer deposition (PALD)] mode, the substrate is exposed to plasma species during the oxidation step, which may serve as a replacement of ligand-exchange reactions typical for NH_3/H_2O deposition, favoring formation of metals, metal nitrides, and metal oxides.[29]

Thin films of NiO_x can be synthesized from different metalorganic/organometallic precursors such as bis(cyclopentadienyl) $Ni(Cp)_2$ with its multiple derivatives,[23,31−41] bis(1,4-do-*tert*-butyl-1,3-diazadienyl) nickel $Ni(tBu_2DAD)_2$,[42] and nickel(II) acetylacetonate $Ni(acac)_2$.[43−46] The synthesis cycle is completed by oxidizing agents (water H_2O or ozone O_3). ALD growth of NiO_x offers room for many improvements. Common metalorganic precursors are usually highly thermally and chemically stable, but they have poor performance in the gas phase, which reduces growth per cycle (GPC) to 0.01−0.08 nm/cycle. Better GPC can be achieved with plasma-assisted ALD that increases the substrate reactivity. Surface adsorption sites should be activated before the deposition process, and correct precursors are to be used for better synthesis flow.[43,47−50]

With such a multitude of control parameters, the improvement of the NiO_x growth process becomes a formidable problem involving multidimensional optimization. Yet one particular subproblem with ALD deposition is especially notorious: the use of the nickel acetylacetonate precursor $Ni(acac)_2$. It has a simple molecular nature and offers good GPC of about 0.07 nm/cycle. On the downside, $Ni(acac)_2$ is very thermally stable, requiring the use of highly reactive oxidizing agents. For ALD NiO, ozone makes a good choice, but it is not necessarily the best oxidizing agent available. Therefore, it is timely and important to perform a systematic comparative study of different oxidizing agents (H_2O, O_3, and O_2), analyzing their influence on the properties of thin NiO_x films obtained with thermal and plasma-enhanced ALD. To simplify the discussion, we used a minimum set control parameters, employing a simple ALD technique without any pre- and post-treatment of the substrates.

2. EXPERIMENTAL SECTION

2.1. NiO_x Synthesis with ALD. Thin nickel oxide films were deposited in a Beneq TFS 200 reactor over glass (Corning microscope slides) and silicon (Si) substrates. Different substrate types were required for characterization of the chemical and physical properties of the resulting material. Substrates were cut into squares 1 × 1 cm^2 (silicon) and 2.5 × 2.5 cm^2 (glass) in size. They were cleaned with acetone and isopropanol (IPA) and rinsed in deionized water (DI), and left for 15 min in an ultrasonic bath during each step. The substrates were dried with industrial-grade nitrogen. Right before mounting the substrate inside the ALD chamber, an additional cleaning with ozone was performed for 15 min. Beneq TFS 200 allows two modifications of ALD to be used: plasma-enhanced ALD (PALD) and thermal atomic layer deposition (TALD). In both configurations, anhydrous (95%) nickel acetylacetonate $Ni(acac)_2$, a sky-blue powder from Strem Chemicals Inc., was used as a precursor. This powder was stored in an HS stainless steel bottle, an equipment accessory used for precursors that require heating for sublimation. The temperature of the bottle was kept at 180 °C for building up the required precursor vapor pressure. We employed the booster mode with 2 s long exposures for keeping the precursor pressure at 2−3 mbar. The principal TALD cycle steps were performed at the chamber temperature of 300 °C as follows: exposure of $Ni(acac)_2$ (3s)—purge with N_2 (2 s)—oxidation (3s)—purge with N_2 (2s). In this case, H_2O and O_3 were used as the oxidizing agents. O_3 was generated in situ by passing oxygen through the ozone generator connected to the reactor. The structural properties of TALD samples suggest that a purge time of 2 s after the oxidation step is sufficient; ref 51 reports even shorter purges for the oxides deposited from acetylacetonate precursors. The PALD cycle, performed at the chamber temperature 220 °C, consisted of: exposure of $Ni(acac)_2$ (3s)—purge with Ar_2 (3s)—oxidation (3s)—purge with Ar_2 (3s). The plasma was produced with a 200 W RF power source with a bias voltage of 25 V. In this case, oxidation was performed with H_2O, O_3, and O_2. The diagrams for both ALD cycles are illustrated in Figure 1. Further on, we use the following abbreviated notation for the samples: T-W and T-Oz designate films grown with TALD under water and under ozone oxidation. P-W, P-Oz, and P-Ox refer to the samples obtained with PALD employing water, ozone, and oxygen as oxidizing agents.

The carrier gas used for the TALD samples was nitrogen (99.999%), while for the DPALD process, argon (99.999%) was employed. The working pressure was maintained at between 50 and 60 Pa. The flow rate of 200 sccm was used for both deposition methods; the gas was flowing from the heated sources to the reaction chamber. Ozone (O_3) was generated from oxygen (99.999%) using the ozone generator BMT803N producing a 200 sccm flow.

2.2. Material Characterization. The thickness of NiO_x films deposited over glass substrates was measured with the specular photoreflectance technique using Filmetrics F20 equipment in the UV−vis range (λ = 300−1000 nm). Optical transmittance and optical band gap were obtained with UV−vis−NIR spectroscopy using an Agilent Cary 5000 spectrometer. Variable angle spectroscopic ellipsometry (VASE) was employed for determining the thicknesses and the principal optical constants of NiO_x films. The ellipsometric parameters were measured with a J.A. Woollam M-2000U instrument under three incidence beam angles (50°, 60°, and 70°). These data were fitted with the Cauchy dispersion equation, characterizing the fit quality with the mean square error. Studies of film morphology were performed using scanning electron microscopy (SEM) with Nova NanoSEM 200

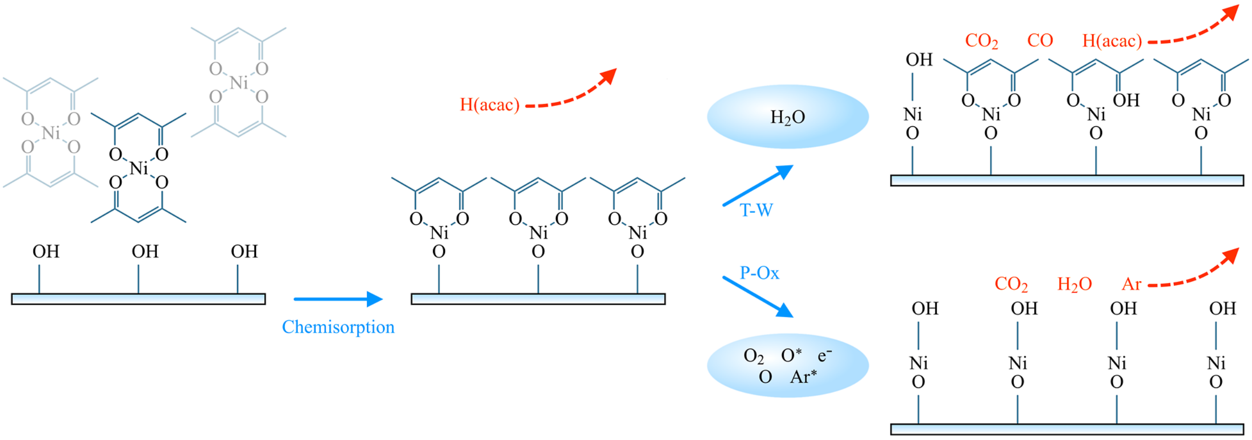

Figure 2. Suggested reaction mechanisms for the thermal and plasma-enhanced ALD using H_2O and O_2 as oxidizing agents.

operating at the accelerating voltage of 15 kV. SEM micrographs were taken with a magnification of 200,000× in several random locations on the sample surface. High-resolution transmission electron microscopy (HRTEM) was carried out with a Nanotech TEM JEOL JEM 2200FS + CS microscope operating at 150 kV. All measurement samples were prepared with the focused ion beam lift-out procedure. Atomic force microscopy (AFM) was employed in tapping mode to analyze the sample surface topography with MFP3D-SA equipment from Asylum Research. The crystallinity of thin NiO_x films was studied with grazing-incidence X-ray diffraction using Panalytical Empyrean equipment with a Cu source (λ = 0.15405 nm). The incidence angle was varied in the range 30–90° with 0.05° steps and ω = 0.7°. The samples were also analyzed with X-ray photoelectron spectroscopy (XPS) to access surface chemistry and stoichiometry. A ThermoScientific ESCALAB 250Xi system (Al K_α = 1486.6 eV) was used with a monochromator. Each XPS spectrum was acquired in 20 scans with a pass energy of 20 eV and an energy step of 0.1 eV. The C 1s core level located at 284.8 eV was used for spectral alignment. Right before the measurements, the sample surface was etched with Ar^+ ions (500 eV) for 30 s. Photoemission spectra of thin NiO_x films were employed for studying the defect subsystem, oxidation state, and relative chemical composition. The individual bands in the spectra were resolved by deconvolution using AAnalyzer software, employing Voigt and Gaussian peak profiles.[52] Prior to deconvolution, the spectrum background was removed using the Shirley and Tougaard procedure.[53] A UV photoelectron spectroscopy (UPS) study was performed with AXIS SUPRA (KRATOS) equipped with a He–I source (21.1 eV). UPS measurements were carried out with voltage bias of −7 V for aligning the Fermi level to the required energy value. Electrical properties of the samples were studied using Hall effect measurements in the Van der Pauw configuration, under the constant current of 10 nA and magnetic field of 550 mT. These measurements were carried out with the Ecopia HMS-3000 equipment at room temperature using 20 nm press-on Au contacts in a square configuration.

3. RESULTS AND DISCUSSION

3.1. Deposition of Nickel Oxide Films with ALD. To obtain high-quality NiO_x films from solid metal–organic precursors, it is important to build up an excess vapor pressure for promoting chemisorption at the film surface. As $Ni(acac)_2$ has considerable thermal stability, the desired vapor pressure can be obtained by heating the precursor container and/or by employing the booster mode, that is, by filling the precursor container with carrier gas from the input valve, keeping the output valve closed while the required pressure builds up. According to the literature, the sufficient vapor pressure of $Ni(acac)_2$ can be achieved for T = 130–230 °C.[28,54−56] It is important to mention a relatively long precursor saturation time (in comparison to other ALD variants available with the TSF 200 equipment[57−59]), which can be attributed to a low reactivity between $Ni(acac)_2$ and the substrate.[46] The main difficulty of using $Ni(acac)_2$ for NiO deposition with any oxidizing agent comes from poor precursor efficiency, requiring a considerable amount of reactant to saturate the surface. This can be attributed to (i) kinetically slow reaction flow under deposition temperatures used (300/220 °C) and (ii) low precursor saturation density, most probably related to steric hindrance of the adsorbed $Ni(acac)_2$ ligands. Taking into account these issues together with equipment operation constraints, we decided to keep the precursor at the constant temperature of 180 °C.

Based on reaction mechanisms proposed by Utriainen et al.,[56] we propose the following reactions for the water-oxidized sample

$$|\text{–OH} + \text{Ni(acac)}_{2(g)} \rightarrow |\text{– O – Ni(acac)} + \text{H(acac)}_{(g)} \tag{1}$$

$$|\text{–O – Ni(acac)} + \text{H}_2\text{O} \rightarrow |\text{– O – Ni – OH} + \text{H(acac)}_{(g)} \tag{2}$$

Here, |– denotes the film substrate and the subscript (g) denotes the desorbed gaseous species. In the first half-cycle (Figure 2), $Ni(acac)_2$ undergoes dissociative adsorption, and free ligand H(acac) is released as a gas; each site is formed by O–Ni(acac). The semireaction resembling eq 1 is reported in the literature for similar molecules deposited with ALD.[46,56,60] The exact reaction mechanism can be revealed only with a dedicated in situ study during the film synthesis; we propose eq 1 as a simplified reaction describing the ideal situation. During the second half of the TALD cycle employing H_2O as an oxidizing agent, water protonates the chemisorbed (acac) ligand, transferring a proton H^+ and releasing acetylacetone H(acac); the generated OH^- leads to the formation of Ni–OH surface species.

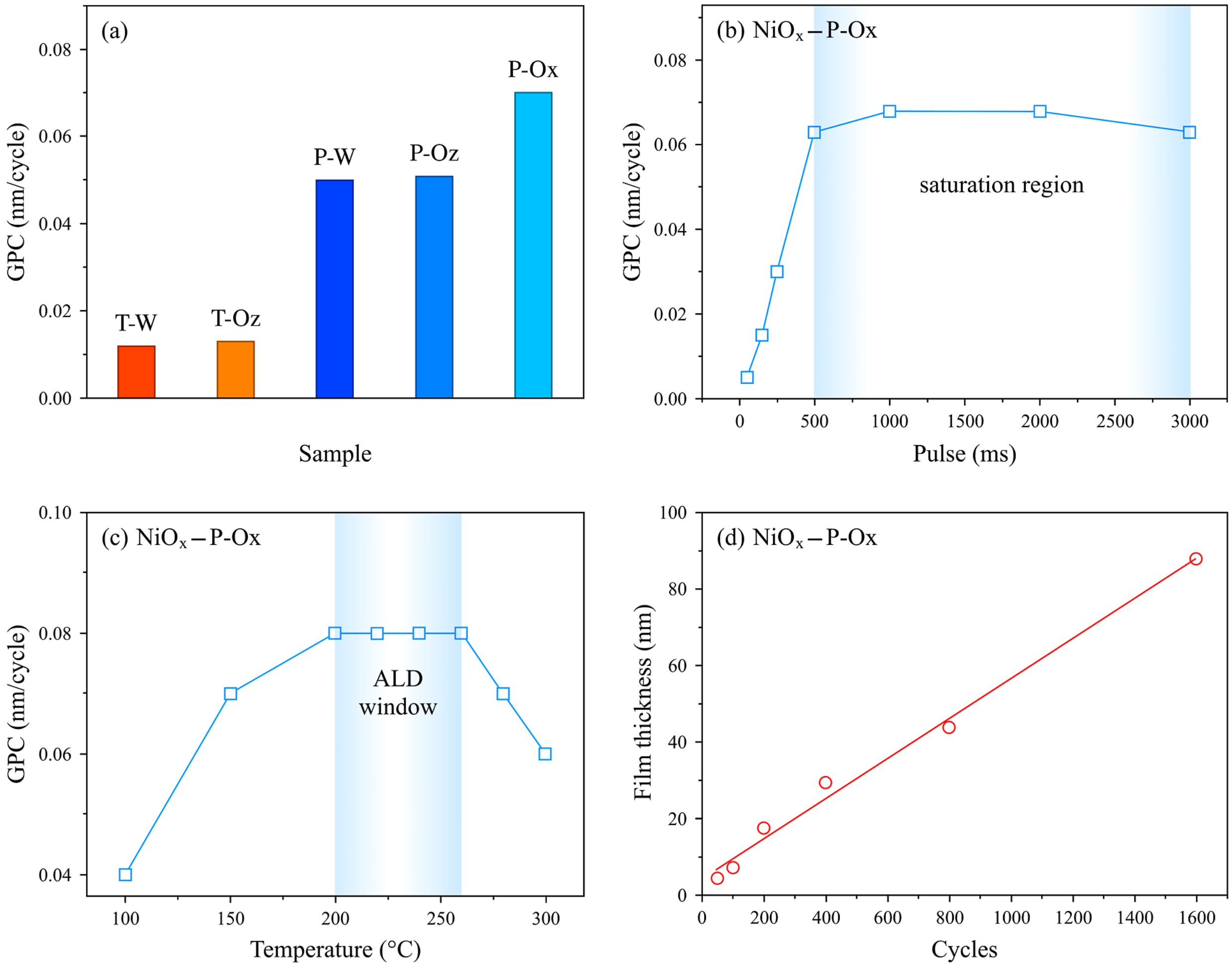

Figure 3. Main characteristics of ALD process: (a) GPC of NiO$_x$ films deposited with 1000 ALD cycles employing different oxidizing agents. (b) GPC saturation region obtained for PALD at 220 °C. (c) ALD window. (d) NiO$_x$ film thickness as a function of cycle number.

Some deviation from this idealized mechanism can occur, since water has an insufficient reactivity for dissociating all acetylacetonate ligands; the latter may remain nondissociated or form ligands with a high carbon content (Figure 2), CO_2 and different oxygen species in the process. CO can be one of the byproducts as well, although we do not include it explicitly in the equations.

The case when plasma from O_2 is used as an oxidizing agent is more complicated due to the presence of several distinct species and plasma radicals at the oxidation step

$$|{-}OH + Ni(acac)_{(g)} + 11/2O_2 + O^* + Ar^* \rightarrow |{-}\ NiO + 7H_2O + 10CO_2 + Ar \quad (3)$$

$$|{-}NiO{+}H_2O + CO_2 + O_2 + 2O^* \rightarrow |{-}\ Ni(OH)_2 + 3O^* + O_2 + CO \quad (4)$$

Here, we suggest simple reactions producing CO_2, H_2O (3), and hydroxyl groups at the sample surface (4). Figure 2 presents a general reaction sketch: the substrate favors formation of H_2O and hydroxyl groups OH during the oxidation step because plasma radicals are highly reactive and have enough power for dissociating nickel acetylacetonate.[29] This mechanism assumes chemisorption of O^{2-} and OH in similarity to water-assisted oxidation (2), with the substantial difference that water is being produced in the second half of cycle (3), favoring the chemisorption of OH that may even become ionized, precluding interchange of the ligand, blocking the oxide growth, and reducing the GPC.

In the P-Oz process, a plasma generator creates an electric field, producing plasma species that interact with ozone molecules. This interaction results in a mixture of oxygen atoms, including ozone molecules (O_3), oxygen molecules (O_2), oxygen ions (O^+, O^-), and excited oxygen molecules (O_2)*. Ozone molecules are inherently unstable and highly reactive, which adds complexity to the process. The use of ozone plasma as an oxidizing agent further complicates the reaction mechanism due to the variety of species generated by the plasma. Given the complexity and the focus of this study, we do not include any detailed reaction mechanism here.

The use of the O_3 plasma requires consideration of several distinct oxygen species and plasma radicals. Utriainen et al.[46] proposed a process composed of the following reactions

$$|{-}OH + Ni(acac)_{2(g)} \rightarrow |{-}\ O - Ni(acac) + H(acac)_{(g)} \quad (5)$$

$$|{-}O - Ni(acac) + 7O_{3(g)} \rightarrow |{-}\ NiO + 10CO_{2(g)} + 7H_2O_{(g)} \quad (6)$$

$$|{-}2NiO + 2O_{3(g)} + 2H_2O_{(g)} \rightarrow |{-}\ 2Ni(OH)_2 + 3O_{2(g)} \quad (7)$$

Here, $Ni(acac)_2$ is dissociatively adsorbed (5), and free ligands are released as gaseous H(acac). In eq 6, the adsorbed ligand is oxidized to CO_2 and H_2O. Finally, at the third step (7) H_2O—a byproduct—adsorbs dissociatively, forming OH^- groups on the film surface. The rate of their formation depends on the availability of oxygen during the intermediate step, which may create an obstacle for efficient film growth.

The type of oxidizing agent determines the degree of $Ni(acac)_{2(g)}$ molecular dissociation and the byproducts formed, influencing the purity and conductivity type of the resulting NiO_x. According to this study, O_2 plasma provides much more efficient oxidation in comparison to the commonly used O_3 and H_2O for both variants of the ALD technique employed. The use of oxygen plasma leads to the formation of water molecules, producing many OH^- groups that interchange with chemisorbed Ni(acac), working in a chemical synergy with the adsorbed O^- groups. This mechanism cannot be achieved when H_2O or O_3 is used as an oxidizing agent. This can be possibly explained by the different chemical environments and reactivities provided by the oxygen plasma compared with H_2O or O_3 oxidizing agents. Oxygen plasma generates a variety of reactive species, including atomic oxygen (O), oxygen ions (O^+, O^-), and radicals like OH^-, which are highly reactive and can directly interact with chemisorbed species at the substrate. This leads to a unique chemical synergy when OH^- groups, produced by the interaction of oxygen plasma with surface species, can readily interchange with chemisorbed Ni(acac) and work in conjunction with the adsorbed O^- groups. The presence of multiple reactive species in the plasma allows for a more complex and effective interaction with the substrate, which may not be possible with H_2O or O_3 alone. Water and ozone primarily introduce oxygen to the surface, but they do not generate the large variety of reactive intermediates (such as OH^- and O^-) with the same level of reactivity and surface interaction. The plasma environment can create a more dynamic and intense surface reaction environment, leading to different mechanisms of film growth or surface modification that cannot be achieved by the simpler oxidative action employing H_2O or O_3. Besides, the catalytic properties of NiO_x may reduce the effectiveness of O_3 as an oxidizing agent, leading to slower growth in the second half of the ALD cycle.

Figure 3a illustrates the GPC for NiO_x films deposited over glass substrates with 1000 ALD cycles. Three clearly marked GPC groups could be observed: the slowest growth with about 0.01 nm/cycle is achieved with the TALD technique. Our GPC values for T-W and T-Oz samples are lower than those reported in the literature, 0.04 to 0.07 nm/cycle.[28,46,61] Such a difference can be ascribed to the insufficient dissociation reactivity during the second half of the ALD cycle. The ideal reaction mechanisms (1, 2) have variations because water and ozone are not reactive enough for dissociating acetylacetonate ligands or for formation of ligands with high carbon content, so that large quantities of reactants are required for saturating the surface. This can be attributed either to kinetically slow reactions under the deposition temperature that we use or to the low surface saturation degree due to steric hindrance produced by the adsorbed $Ni(acac)_2$ ligands. The straightforward solution would be to employ higher reaction temperatures, which will enable the Arrhenius law for reaction kinetics with the rate $\propto \exp(-1/T)$, favoring dissociation of the $Ni(acac)_2$ molecule in the gas phase. However, this solution was not suitable for the present study: we sought to produce good-quality films for optoelectronic applications that may require deposition over flexible substrates. This requirement is not compatible with increased deposition temperatures.

The GPC can certainly be increased by adjusting the exposure times of the metal precursor and performing a saturation study. This extra step was not made here for enabling more straightforward comparison of the samples. Particularly in the case of T-Oz, our argument is based on the potential catalytic decomposition of O_3 by NiO, which, despite being already reported in the literature, still requires further investigation and more precise understanding of its role in the growth process.

A higher GPC of 0.05 nm/cycle was obtained for P-W and P-Oz samples. The largest GPC of 0.07 nm/cycle was achieved with the PALD technique using O_2 plasma as the oxidizing agent, which was possible due to the enhanced reactivity of $Ni(acac)_2$ exposed to plasma radicals that reach down to the substrate.[29] One can assume that in the PALD mode, the second half-cycle promotes formation of hydroxyl groups/radicals on the surface (4) under the action of plasma (Figure 2).

To achieve a better understanding of the deposition procedure employing O_2, we determined the ALD saturation region (Figure 3b) by synthesizing various NiO_x films under the same conditions over glass substrates, varying only the length of $Ni(acac)_2$ exposure. As one can see, GPC increases linearly for pulses of 50−250 ms. Saturation takes place for 500−3000 ms pulses, bringing GPC almost to 0.07 nm/cycle. This behavior is expected when the volume of gas adsorbed by metallic precursor increases, saturating GPC for pulse lengths of 500 ms and above. The obtained GPC of 0.068 nm/cycle is defined by the steric hindrance of precursor. Our GPC values are larger than those provided in the literature.[24]

For the temperatures 100−200 °C and 1000 ms $Ni(acac)_2$ pulses, we obtained the GPC of 0.04−0.08 nm/cycle. The ALD temperature window was found at 200−260 °C (Figure 3c) with a constant GPC of 0.08 nm/cycle. The decrease of GPC at higher temperatures can be explained by reduction of hydroxyl groups at the film surface, producing denser NiO_x material due to a thermally activated dihydroxylation reaction. A similar behavior was observed for Nickel bis-(methylcyclopentadienyl) $Ni(MeCp)_2$ oxidized with O_2 plasma.[22,29] The thickness of our films depends linearly on the number of cycles (Figure 3d). To produce this plot, we used the same $Ni(acac)_2$ exposure of 1000 ms and substrate temperature of 220 °C. Higher reaction temperature favors gas phase dissociation of $Ni(acac)_2$. Figure 3 proves that the P-Ox technique is the best for obtaining stoichiometric NiO_x films in the given ALD temperature window (Figure 3c). The successful deposition results from oxidation synergy between adsorbed OH^- and O^- groups as well as from interchange of ligands with the chemisorbed Ni(acac). This superficial chemistry is not available for H_2O or O_3 oxidation agents. The formation of OH ionized groups and high density of ionized oxygen species also improve the dissociation of $Ni(acac)_2$ and molecular derivatives thereof.

In the PALD process employing oxygen or ozone, plasma may feature different reactive species: O_2 molecules, atomic oxygen, oxygen radicals, and O_2^+ ions. Each of them plays a different role in the deposition process. Ions—oxygen cations O^+ and anions O^-—crash against the substrate, causing variations in film density, modifying local film adhesion, producing areas of mechanical stress, and even promoting surface degradation and etching. Radicals—atomic oxygen and $O_2^{\bullet}$—are highly reactive due to having unpaired electrons; they facilitate chemical reactions required for the film growth. Radicals and ions interact with precursor molecules at the different stages of PALD cycle.

3.2. Structural Analysis. Figure 4 shows the GIXRD spectra of NiO_x films formed with 1000 ALD cycles on glass substrates using different oxidizing agents. The spectra of TALD and PALD films are different: TALD films are crystalline, while PALD ones are more amorphous. The latter stems from the use of lower deposition temperature (220 °C), under which the activation energy is insufficient for forming large crystals, which contrasts with the TALD samples obtained at 300 °C. Although plasma-assisted synthesis favors film growth due to higher reactivity of OH and O radicals, thermal differences may lead to changes in the nucleation and crystallization mechanisms.

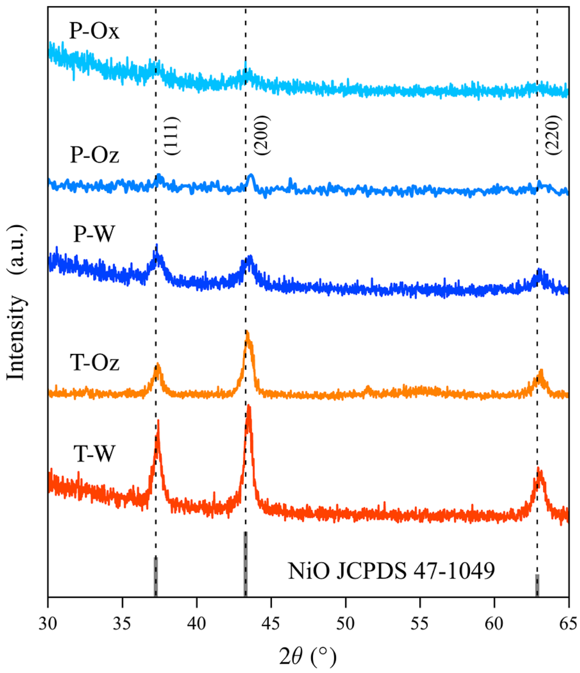

Figure 4. GIXRD patterns for the thin NiO_x films. The JCPDS 47-1049 card corresponds to the FCC crystalline NiO.

These results differ from those reported,[56] where crystalline particles were obtained with the P-Oz technique. Despite ozone being very reactive, considerable doses of precursor were required for saturation of the film surface at 250 °C, which indicates relatively slow reaction kinetics. In the present study, all NiO_x films are polycrystalline. Their spectra feature three reflection peaks corresponding to the (111), (200), and (220) directions of the NiO lattice, respectively. Such a combination of peaks is characteristic of the symmetry group $Fm\bar{3}m$. In accordance with reference card JCPDS 47-1049, we identified the peak pattern in question with a rock-salt cubic structure. The most pronounced (200) peak does not coincide with the principal reflection. This issue is characteristic of the FCC phase, where the energy of the (100) surface plane turns out to be the lowest. Although plasma-assisted synthesis is beneficial because of the higher reactivity of ionized OH and O, it may also influence nucleation and crystallization mechanisms.

Therefore, chemisorbed species can be desorbed back when plasma ions clash with the film surface. The lower crystallinity of PALD films also stems from insufficient plasma energy that fails to maintain the ordered crystalline growth due to short surface diffusion lengths.[14,25,28,62−64] None of the ALD films produced in this study displayed peak patterns corresponding to pure Ni or Ni_2O_3. The size of crystallites corresponding to the (220) peak can be estimated with the Scherrer formula, yielding the values of 12.24 and 14.4 nm for T-Oz and T-W samples, respectively. This result suggests that, independently on the oxidizing agent involved, the crystallites are very small. The general degree of disorder increases when using plasma-assisted deposition. The size of the crystallites is defined by a low intrinsic GPC characteristic for $Ni(acac)_2$; further limitations are imposed by the low synthesis temperature.

To study the thickness of the interface layer, we made several HRTEM cross-sectional images of the representative NiO_x films (Figure 5). The thicknesses of these films are

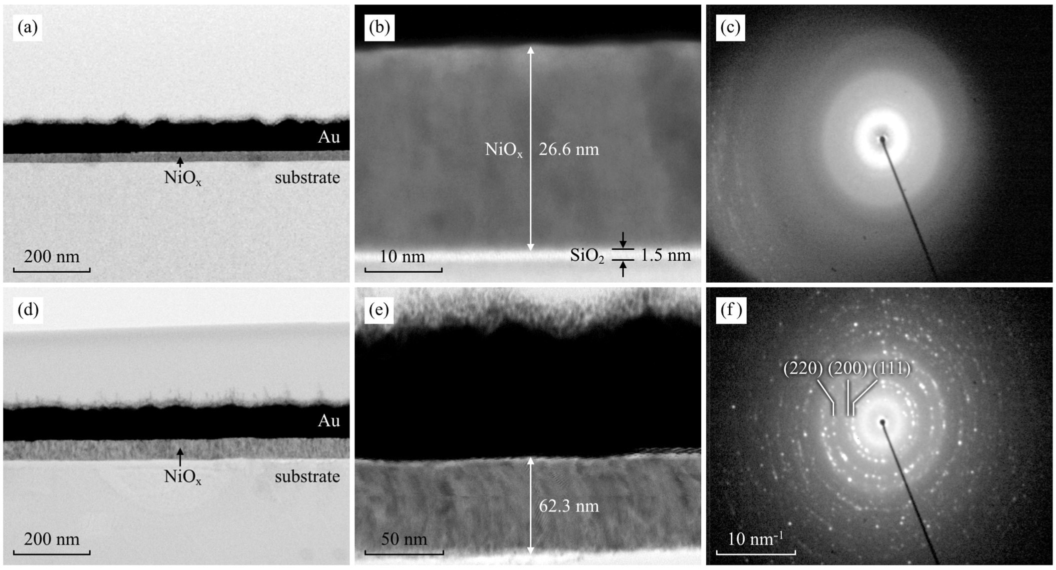

Figure 5. Cross-sectional HRTEM and X-ray diffraction patterns for thin NiO films grown with (a−c) P-Oz and (d−f) T-W.

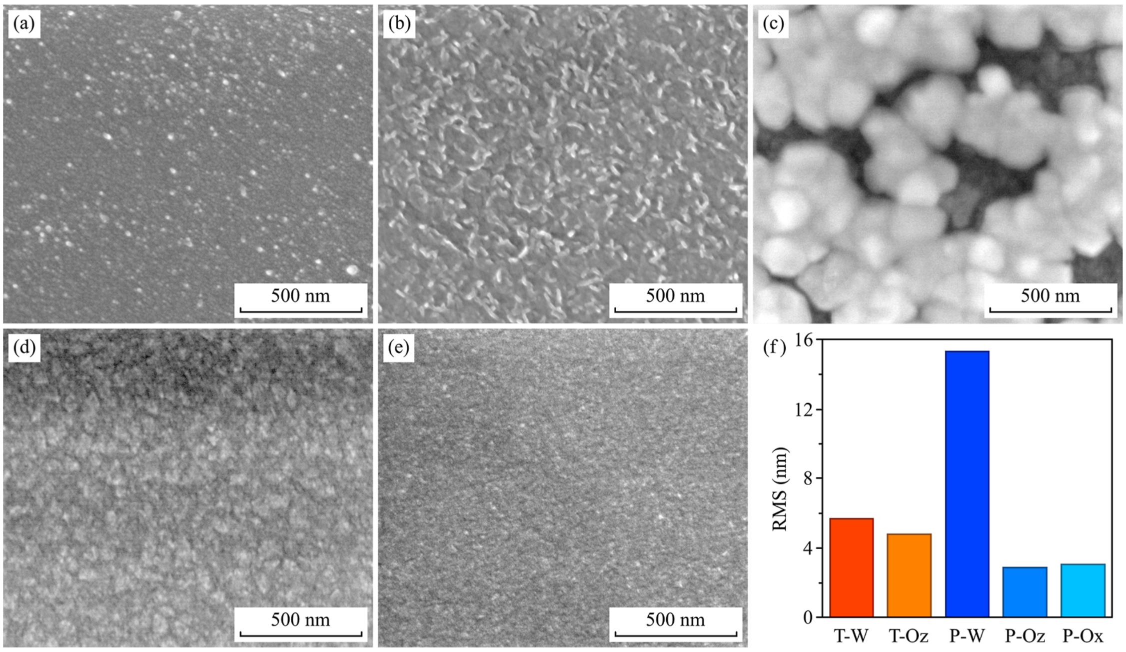

Figure 6. Top-view SEM micrographs of thin NiO_x films deposited with different ALD techniques and distinct oxidizing agents: (a) T-W; (b) T-Oz; (c) P-W; (d) P-Oz; (e) P-Ox; (f) film surface RMS obtained from AFM studies. Approximate film thickness: (a,b) 12; (c–e) 50 nm.

distinct because TALD and PALD processes usually produce different GPC values. We compare a sample prepared by TALD (62.3 nm) with one prepared by PALD (26.6 nm) using the HRTEM and Electron Diffraction (ED) analyses. In spite of a distinct thickness, our results highlight the main crystallographic differences between the films obtained by thermal ALD and plasma ALD syntheses: the crystallinity degree of the TALD samples is higher, which is further corroborated by XRD (Figure 4) and SEM (Figure 6). The interface SiO_2 layer about 1.5 nm thick is formed between the NiO film and the silicon substrate (Figure 5b). PALD produces films with the overall structure similar to that of TALD films. All films have good adhesion to the surface and a uniform thickness through the cross section analyzed; the growth of NiO_x is conformal. Film thicknesses obtained with TEM analysis coincide with the values measured using spectral reflectometry with a Filmetrics setup.

PALD and TALD samples differ slightly in terms of their crystallinity degree. Although both are polycrystalline, PALD samples are less crystalline (Figure 5a–c) than the TALD samples (Figure 5d–f). The Selected Area Electron Diffraction (SAED) pattern (Figure 5f) reveals more crystalline regions for the T-W sample when compared to the P-Oz sample, which shows amorphous regions (Figure 5c), which is consistent with the XRD results. In HRTEM images, one can observe columnar growth of small crystals oriented in the ⟨200⟩ direction. Several diffraction rings are visible in SAED images (Figure 5c,f) for all of the films studied. Figure 5f shows that interplanar spacings along the (200) and (111) planes are 2.1 and 2.4 Å, respectively, which is consistent with the crystalline structure of FCC NiO.

Direct plasma ALD, particularly in the case of H_2O plasma, employs high-energy ions and radicals that may significantly affect film morphology and crystallinity, with the potential of causing surface damage and disrupting lattice regularity, resulting in films with different properties in comparison to those obtained with lower-energy methods. Amorphous or low-crystalline regions observed in this study illustrate this point to perfection.

3.3. Film Morphology and Surface Topography.

Figure 6 shows SEM micrographs of NiO_x films deposited on glass substrates with different ALD techniques and oxidizing agents. Surface morphology depends strongly on the ALD variant and the type of oxidizing agent used. There is a marked difference in packaging density and geometry of the surface particles observed in the top view. The features of T-W and T-Oz samples can be explained as an effect of steric hindrance and low synthesis temperature, which reduces nucleation intensity. The PALD process is more reactive, which is apparent for the P-W sample featuring large and well-defined crystals about 150 nm in size; these can appear only under advanced molecular dissociation of the precursor. In this case, surface coverage is far from being uniform with a considerable number of pinholes. Although surface particles are large, their aggregates have a metallic character that can be detected with XPS.

The literature reports that plasma-enhanced ALD typically generates O^-, OH^-, and H^- radicals as subproducts.[29] Among these reactive species, H^- radicals require special attention: according to the theoretical study of hydrogen-assisted deposition of $Cu(acac)_2$,[60] hydrogen molecules can break metal–oxygen bonds. From this perspective, with H^- radicals appearing in the second half of the ALD cycle, metal–oxygen bonds may break uncontrollably, producing a mixture of metallic nickel with nickel oxide. This problem can be resolved by employing longer purge steps and/or reducing plasma exposure time. In other words, water plasma favors reduction to the oxidation process; thus, hydrogen ions can reduce Ni(acac) molecules,[60] leading to uncontrolled growth of metallic Ni and NiO_x.[65] Detailed understanding of this process can be obtained only with an ample dedicated study that goes beyond the scope of the present paper.

The larger degree of surface packing is evident for P-Oz and P-Ox samples in comparison to the P-W sample. This can be attributed to the action of ionized hydrogen species and the elevated density of OH groups, upsetting the molecular interchange balance at the film surface. This phenomenon can be visualized with a simple geometrical model described by Ylilammi.[66] In terms of the optimal surface topography required for the hole transfer layer (HTL) layer, PALD synthesis with O_2 plasma and O_3 plasma is more recommendable. In general, except for the P-W sample, PALD permits us to obtain continuous and defect-free films with a homogeneous surface. The surface structures observed here are fully consistent with those reported in the literature for CVD- and ALD-synthesized NiO films.[25,67]

Similar conclusions about film morphology can be obtained from the AFM data (Figure S1), which were used to determine the root-mean-square (RMS) roughness of the surface formations (Figure 6f). The higher roughness is observed for thermally deposited samples: 5.72 and 4.75 nm for T-W and T-Oz films, respectively. Such large roughness is expected for grains formed at random, due to high atom mobility during the thermal decomposition of $Ni(acac)_2$, as it is the case of $NiCp_2$.[68] Steric hindrance may also contribute to the heterogeneous nature of the T-Oz and T-W samples. Plasma-assisted film deposition produces slightly lower RMS: 2.83 and 3.09 nm for P-Oz and P-Ox samples, respectively. The P-W sample features the record RMS of 15.36 nm due to irregular surface morphology with large grains and pinholes (Figure 6c). Judging from the RMS data, the films obtained with ozone and oxygen plasma are of the best quality due to the low number of defects and high surface coverage degree.

PALD synthesis (and in particular P-W) introduces much surface roughness. The high kinetic energy of the ions (H_3O^+, OH^+) and radicals ($OH^\bullet$, $H^\bullet$) allows them to reach the substrate, causing physical impact damage (forming pits) and producing numerous surface defects.

3.4. Surface Chemistry of Nickel Oxide Films.

Just before the measurements, the surface of the samples was etched with Ar^+ ions (500 eV) for 30 s. Photoemission spectra of thin NiO_x films were employed for studying the system of defects, oxidation state, and the relative chemical composition. The C 1s core level located at 284.8 eV was used for spectral alignment. High-resolution spectra corresponding to C 1s, Ni 2p, and O 1s were deconvoluted using AAnalyzer software with Voigt and Gaussian peak profiles.[52] Prior to this, the spectrum background was removed following the Shirley and Tougaard procedure.[53] The core levels were correlated to the main peaks to keep the FWMH constant for every component. The fitting of the Ni 2p core level was performed using spin−orbit splitting data. To calculate the Ni/O ratio, it was important to distinguish chemical bonds with overlapping binding energies, a consequence of the similar electronegativity of the nearest-neighboring atoms. The literature is somewhat uncertain about the positions of the O 1s bonds, specifically those corresponding to the energy range 531−532 eV where oxygen vacancies, hydroxyl, and covalent bonding peaks overlap. For this reason, a deconvolution analysis was carried out with the minimum number of peaks, applying the corresponding peak intensity corrections.

Figure 7 shows the C 1s photoemission spectra of NiO_x films. The C 1s spectrum was accounted for as contributions from adventitious carbon (C−OH/C−O−C and O−C═O). These bonds have peaks at 286.1 and 288.8 eV; they are usually produced by $Ni(acac)_2$ reaction byproducts. The calculated chemical composition confirms a high concentration of carbon in the T-W and P-W films (Table 1). The presence of superficial carbon may be attributed to the insufficient dissociation of $Ni(acac)_2$ (Figure 2); the larger contamination degree (52 at. % of C) is observed for the T-W sample (Table 1).

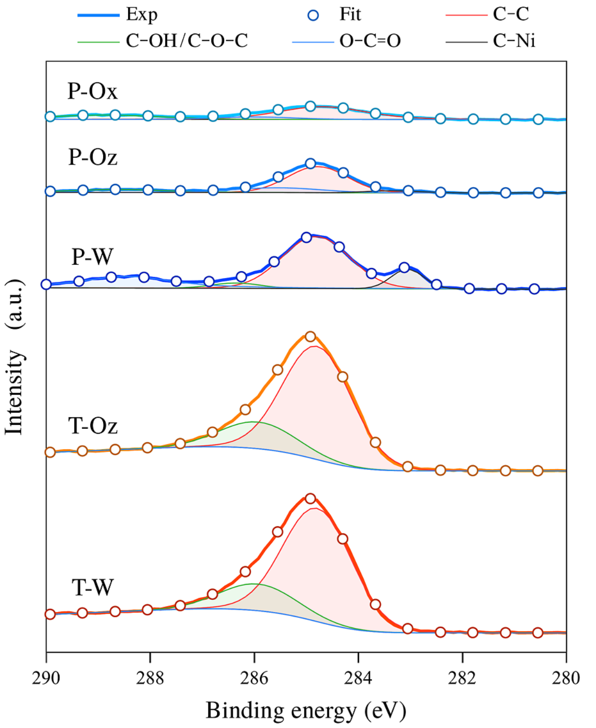

Figure 7. XPS spectra of NiO_x films deposited by ALD and PALD methods using different oxidation agents. The C 1s signal is deconvoluted into four partial contributions.

The carbonyls (O−C═O) are present with concentrations of about 1−7 at. %; no marked distinction in carbonate content for TALD and PALD samples was observed. The largest concentration of the tetra-oxazoline atom corresponds to the P-W sample, which stands out with its rougher surface and pronounced formation of metallic nickel. Fine-tuning and controlling of carbonate content is an important issue for the further optimization of NiO_x deposition techniques, which may produce better electrical properties and enhance electronic structure of the films, improving their HTL performance in solar cells. It is supposed that H_2O dissociates Ni(acac), forming NiOH (2). A possible way of achieving better efficiency of thermal synthesis concerns increasing reaction temperature to reach the level when the Arrhenius law for the reaction kinetics rate $\propto \exp(-1/T)$ can be assumed. In the present study, we did not follow this route, aiming on optoelectronic applications that may require deposition on flexible substrates that do not permit excessively high temperatures. Contaminant concentration is much reduced for PALD films with the oxidation step favoring dissociation of $Ni(acac)_2$. The resulting films feature lower degree of contamination in comparison to those reported in the literature.[25,68] The P-Ox sample had the lowest contaminant concentration (Table 1). We assume that ionic oxygen O^{2-} serves most efficiently for dissociation of chemisorbed Ni(acac) in reaction (4). Water plasma can be exceedingly reactive, as witnessed by the P-W sample with surface particles in excess of 100 nm in size, which, moreover, have metallic character according to XPS. In contrast to the thermal

Table 1. Atomic Composition of NiO_x Films

sample	Ni^0	Ni^{2+}	Ni_{def}	O	O^{-2}	O_{def}	C	O−C=O	Ni_{def}/O^{2-}	Ni/O ratio
T-W	0	20	6	3	6	9	52	4	1.00	1.44
T-Oz	0	20	14	29	15	4	17	1	0.93	0.71
P-W	3	13	17	24	13	5	21	7	1.30	0.71
P-Oz	0	26	12	37	10	1	12	2	1.20	0.79
P-Ox	0	27	16	34	11	1	8	3	1.45	0.93

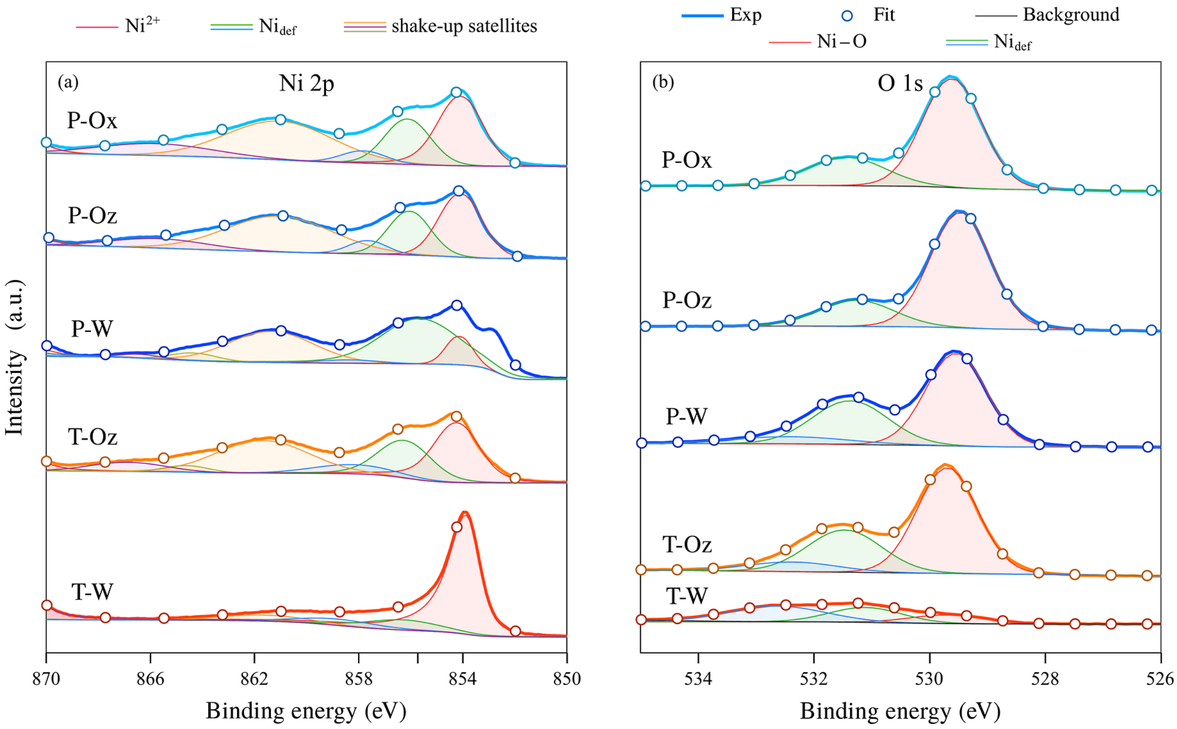

Figure 8. Photoemission spectra for NiO_x films: (a) Ni 2p core level; (b) O 1s core level.

synthesis assisted with H_2O, water plasma favors dissociation of Ni(acac) in the presence of different ionized species of O and OH. This particular behavior of H_2O plasma limits oxide formation and favors formation of metallic Ni.

Figure 8a presents photoemission spectra for the Ni 2p core level. All samples feature a complex set of multiplets characteristic to transition-metal oxides and hydroxides, which complicates the identification of individual peaks. Our equipment permitted experimental measurement of peak positions with the precision of ±0.3 eV. Six characteristic peaks were identified at 854.3, 856.1, 858.3, 861.6, 864.8, and 866.8 eV; they correspond to nickel oxidation states Ni^{2+}/Ni^{3+} and shakeup satellites.[69]

The Ni 2p signal can be associated with nickel configurations $3d^{10}L^2$ (Ni^{2+} contribution) as well as $c3d^8$ (Ni^{2+} of $Ni(OH)_2$), $c3d^9L$ (both corresponding to Ni^{3+}), where the letter "c" represents a hole located at the 2p level-core and "L" corresponds to a hole associated with the ligand bond.[70,71] The knowledge of nickel configurations permits a better understanding of anion−cation coordination in this material. All Ni 2p photoemission spectra shown in Figure 8a feature the Ni^{2+} signal. The shakeup satellites and signal related to charge transfer (bands located about 1.8 eV away from Ni^{2+} peak) are caused by chemical displacement of Ni^{2+} in $Ni(OH)_2$ taking place at the film surface,[72,73] which confirms the presence of hydroxyl groups. Three main bands associated with the Ni^{2+} and Ni^{3+} doublet are shifted by about 17.6 eV. The peak located at 854.3 ± 0.3 eV can be ascribed to Ni^{2+} ions aligned into octahedral NiO_6 crystalline cell, identifiable with a cubic rock-salt phase of NiO.[71,74,75] This type of symmetry was obtained for all XRD spectra reported here.

Identification of transition metals' chemical states from their 2p XPS spectra is a challenging task because of the multiplet splitting, shakeup effects, and plasmon loss structures. On top of that, the peaks corresponding to different chemical states frequently overlap. The prominent databases (e.g., NIST, Phi Handbook) attempt to identify oxidation states based on the $2p_{3/2}$ binding energies, which assumes a single-peak signal. This assumption often fails for the transition metals like Ni, where accurate multiplet assignment is crucial for quantitative analysis. Careful and consistent fitting procedures are paramount.[76]

The peak located at 856.1 eV remains controversial; some literature sources attribute it to Ni^{2+} ($Ni(OH)_2$), others to Ni^{3+} (Ni_2O_3), and yet others to a mixture of both. The main problem with Ni^{3+} concerns its general instability; under normal conditions, it tends to reduce into Ni^{2+}. In some cases,[77−80] the identification of Ni^{3+} species is contestable because multiplet effects are not properly accounted for. Although ref 73 provides a convincing evidence for Ni^{3+}, it concerns a very special case of potassium doping. At the same time, under extremely favorable conditions, such as PALD synthesis with an abundant oxygen supply or under elevated temperatures, the formation of Ni_2O_3 is possible. The papers

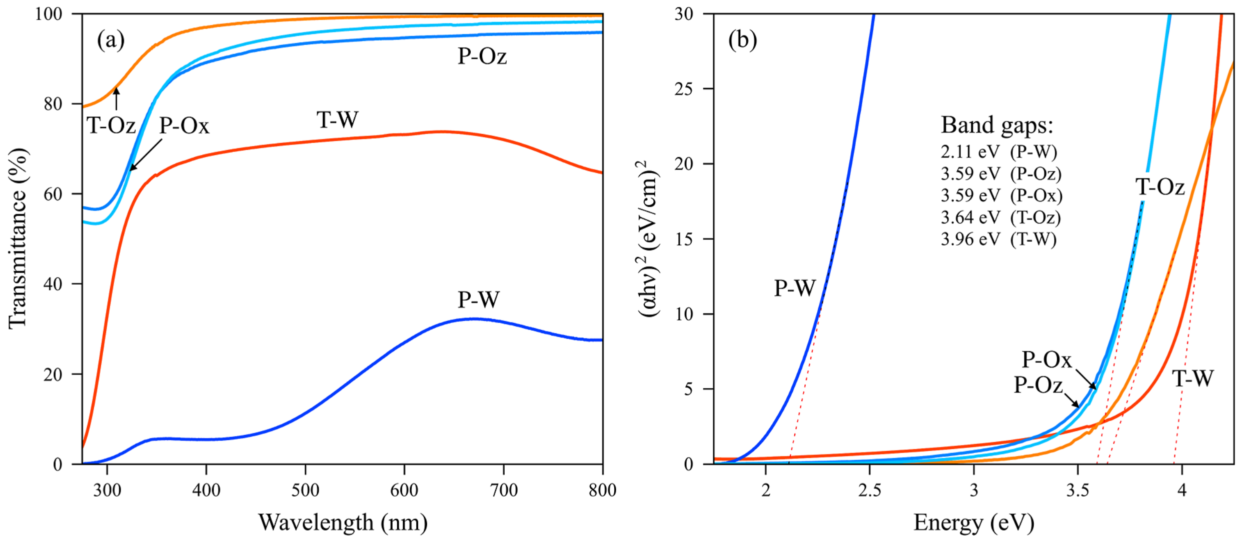

Figure 9. Transmittance spectra (a) and Tauc plots (b) for the thin NiO_x films.

that report contrasting results[69,76,81−84] have a good theoretical foundation and are widely accepted by the community, suggesting that the peak in question is produced by NiO (Ni^{2+}) with the multiplet effects in play.

Taking all this complexity into account, we consider the 856.1 eV peak as a contribution from Ni^{2+} located at the surface defects $Ni(OH)_2$,[76] which have an octahedral configuration and are formed by hydroxyl groups during the second half of the ALD cycle (1−7). This interpretation rules out the formation of Ni_2O_3. The 858.3 eV peak is attributed to NiOOH groups of pyramidal shape, which contain Ni^{3+}. In this way, the discussion gets to the point of differentiation between NiO, NiOOH, and $Ni(OH)_2$. Although the exact attribution of Ni^{2+} and Ni^{3+} species has a considerable importance for material science, we do not attempt it here because the present paper is focused on the NiO_x films serving as a component for perovskite solar cells. To simplify further discussion, we join both Ni^{2+} and Ni^{3+} contributions under the umbrella term "nickel defects" in Ni_{def}.

The shapes of photoemission spectra make a clear distinction between the different oxidizing agents employed. If oxidation was performed with water in PALD or TALD mode, the Ni 2p core level becomes affected due to insufficient oxidation and incomplete reactions.

The peak located at 852.9 eV (P-W sample) suggests the presence of metallic Ni (Ni^0) in NiO_x films, likely coming from hydrogen reduction in water plasma.[60] This sample also features a very low Ni/O ratio (0.71), highlighting the efficiency of the O and OH radicals in dissociating chemisorbed Ni(acac), which leads to overoxidation and oxygen excess in P-W synthesis. In contrast, the higher Ni/O ratio in T-W samples (1.41) suggests a lower degree of oxidation compared to P-W samples, possibly due to differences in plasma reactivity.

P-Ox synthesis produced the best-quality films in terms of the Ni/O ratio. We assume a larger efficiency of ionic oxygen O^{2-} for dissociation of chemisorbed Ni(acac) and metal oxidation in accordance to eq 4. There are subtle differences between H_2O- and O_2-plasma oxidation mechanisms. The P-Ox synthesis, in contrast to P-W, triggers a superficial reaction favoring ligand interchange due to the presence of hydroxyl radicals produced from water generated as a byproduct in the P-Ox cycle.

To improve interpretation of Ni 2p spectra, Figure 8b provides the O 1s core level for all NiO_x samples studied. The photoemission peak at 529.6 ± 0.2 eV is associated with NiO; if defects and/or distortions are introduced to the crystalline lattice, this peak shifts to 531 ± 0.2 eV. The band at 533 ± 0.3 eV (appearing in deconvoluted T-W, T-Oz and P-W spectra) can be related to the defects formed during the oxidation step.

In particular, for water-assisted oxidation, the concentration of O and C increases due to low water reactivity in the presence of $Ni(acac)_2$, which is caused in part by the presence of contaminants at the film surface. The spectrum for the T-W sample has the smallest Ni−O contribution, leading to high Ni/O ratio (1.44) indicating the excess of Ni (or deficiency of oxygen). Plasma deposition of P-W samples effectively reduces the Ni/O ratio to 0.71, offering a potential advantage over traditional thermal synthesis methods in terms of oxygen control. In general, all plasma-assisted methods outperform TALD in metallic oxide formation.

Importantly, the P-Ox film features a far lower concentration of contaminants, producing a Ni/O ratio of 0.93 (Table 1); the next best is the P-Oz sample with a Ni/O ratio of 0.79 (Table 1). We attribute these values, approaching the expected stoichiometry Ni/O = 1, to the use of the O_2 plasma and the O_3 plasma, which favors dissociation of Ni(acac) through formation of concentrated OH^-. If the latter becomes ionized, molecular interchange reactions are further improved. The synthesis of NiO_x under temperatures lower than 220 °C is favored by the plasma of oxygen (to a larger degree) and ozone (to a moderate degree). The conventional water-assisted synthesis results in suboxidation and production of carbon in excessive concentrations.

3.5. Optical Properties.

The influence of the oxidizing agent on the NiO_x band gap was studied using optical transmission measurements (Figure 9) for films with a thickness of 10 nm. All samples are reasonably transparent in the visible range with a decrease in transparency observed for NiO_x films deposited with water oxidation. The highest transmittance was obtained for the T-Oz and P-Ox films, with maximum values reaching 97% and 92%, respectively. In both cases, transmittance over 80% is maintained for almost the entire visible range. This result is extremely important for photovoltaic applications where NiO_x can be used as a hole transport material. The P-W sample features the lowest transmittance value (<30%) in the spectral range analyzed, which is explained by its nonstoichiometric nature. The band gap E_g of the films was calculated with the Tauc method, which involves extrapolation of the linear portion of the absorption coefficient curves to an intersection with the energy axis; it was assumed that all films have a direct band gap. In all cases, it was possible to achieve a linear fit in the Tauc plot with the exponent of 2. No fitting was possible with the exponent of 0.5, which is used for indirect band gap materials. The resulting E_g estimates for T-W, T-Oz, P-W, P-Oz, and P-Ox samples are 3.96, 3.64, 2.11, 3.59, and 3.59 eV, respectively. These values are consistent with the literature data for NiO_x films deposited using CVD and ALD methods.[62,67] The band gap of the P-W sample deviates due to the presence of metallic Ni and high carbon concentration at the film surface. The P-Oz and P-Ox samples exhibit smaller E_g values, which may be associated with transitions to impurity levels located inside the band gap, formed by the excess oxygen vacancies in p-type NiO_x. These results highlight the pronounced dependence of the oxidizing agent on the optical band gap, which may permit efficient tuning of E_g.

We suggest that variations in visible optical transmittance are governed by the type and density of defects in NiO_x films, which are influenced by the oxidizing agent used. The choice of oxidizing agent determines the degree of $Ni(acac)_{2(g)}$ molecular dissociation and the byproducts formed, thereby influencing the purity of the resulting NiO_x films. This study indicates that O_2 plasma provides significantly more efficient oxidation compared to the commonly used O_3 and H_2O for both ALD variants employed here. The use of oxygen plasma leads to the formation of water molecules, producing numerous OH^- groups that interact with chemisorbed Ni(acac) and create a chemical synergy with the adsorbed O^- groups. This mechanism is not possible when H_2O or O_3 is used as an oxidizing agent. Extreme cases, such as P-W synthesis, promote the complete dissociation of the precursor molecule, resulting in a metallic film of significantly reduced transparency, yielding the lowest transmittance value under 30% in the spectral range 300−800 nm.

The samples were further studied with variable-angle spectroscopic ellipsometry (VASE) analysis, measuring the parameters Psi Ψ and Delta Δ under different light incidence angles for the P-Ox sample to determine film thicknesses and its principal optical constants (Figure S2a). Please consult the Supporting Information for a more detailed discussion. The resulting optical constants *n* and *k* are plotted in Figure S2b; their numerical values for the wavelength 632.8 nm are given in Table 2.

The values of refraction index n for the P-Ox sample match reasonably well with those reported in the literature for NiO_x films.[22,85,86] Film thicknesses determined via ellipsometry, specular photoreflectance, and TEM agree for the T-Oz, P-Oz and P-Ox samples. Any differences observed can be explained in terms of composition differences and distinct Ni/O ratio. Refraction index decreases by a factor of 2 in the wavelength range 500−600 nm. Our analysis (results not included) suggests that n is proportional to the film density, which is the largest for P-Oz and P-Ox samples.

The samples with the highest transparency, T-Oz and P-Ox, exhibited the lowest refractive indices of 1.8 and 1.99, respectively, and had the lowest percentage of carbon impurities. The P-Oz sample exhibited the highest refractive index, which is associated with the moderate presence of carbon impurities, as observed by XPS. It was impossible to fit the experimental data for the T-W and P-W samples using the simple Cauchy model, which is possibly related to the higher concentrations of carbon and nickel, resulting in significant absorption within this wavelength range. A very small extinction coefficient *k* for λ = 400−1000 nm (Figure S2b) is indicative of high film transparency in this part of the spectrum. Similar values of k were obtained for the samples deposited with T-Oz, P-Oz, and P-Ox. The absorption tail extends from the band edge of 375 nm (~3.31 eV) to about 410 nm (~3.02 eV). It can be caused by excitonic effects or electron transitions between the valence/conduction band and the shallow defect/impurity energy levels formed inside the band gap. No detailed physical mechanism was proposed for a description of these phenomena yet. However, we can state that the P-Ox sample, despite having an absorption tail, features the best optical transparency among the films obtained in this study.

Table 2. Optical Constants Defined from Ellipsometric Data

sample	*n* (λ = 632.8 nm)	*k* (λ = 632.8 nm)
T-W		
T-Oz	1.80	6.14×10^{-5}
P-W		
P-Oz	2.32	0.10
P-Ox	1.99	4.83×10^{-5}

3.6. Electrical Properties.

The different film thicknesses do not impact significantly their electrical properties because the latter were measured over a nonconductive substrate—glass—producing electrical response from the films only. Figure 10 shows the principal electrical parameters: resistivity, mobility, and carrier concentrations of the NiO_x films studied. As one can see, PALD and TALD samples differ considerably. With plasma-assisted synthesis, one obtains a p-type material with high carrier mobility μ. The largest mobility of 96.38 $cm^2/V{\cdot}s$ corresponds to an n-type P-W sample with excess metallic Ni, which does not qualify as a good NiO_x film for photovoltaic

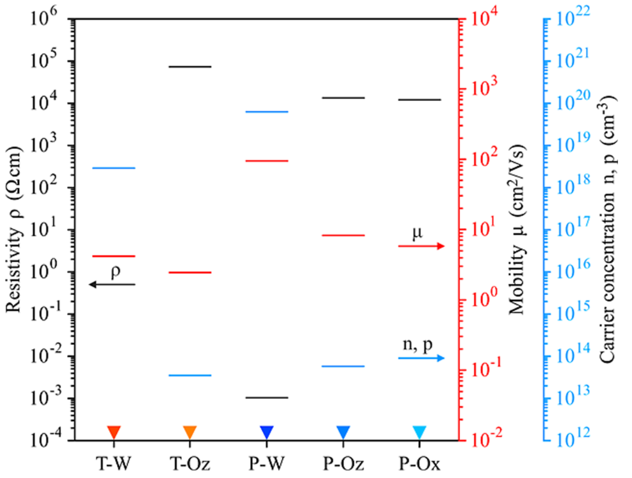

Figure 10. Resistivity, mobility, and carrier concentration for ALD NiO_x films.

applications. The second largest—yet much lower—mobility of 8.28 $cm^2/V \cdot s$ was observed for the p-type P-Oz sample, which can be explained by low carrier concentration ($p \sim 10^{13}$ cm^{-3})—a consequence of low density of defects in the band gap. The P-Ox synthesis also provides a good degree of semiconductor oxidation and the best stoichiometry, which impacts its resistivity value ($\rho = 1.18 \times 10^4$ Ω·cm). The films grown under H_2O-oxidation are different due to the elevated concentration of carbon at the film surface, which considerably lowers their resistance (5.15×10^{-1} Ω·cm and 1.04×10^{-3} Ω·cm for T-W and P-W samples, correspondingly). The electrical properties of thin films are known to be directly influenced by their chemical composition and crystallinity. Nonetheless, these properties can also be altered by the introduction of defects or dopants.

Our results suggest that the introduction of cation defects Ni_{def}, associated with the hydroxyl groups in $Ni(OH)_2$ and Ni^{3+} species, can significantly improve the electrical conductivity of NiO_x films.[87,88] Notably, our films demonstrate a synergistic interaction between nickel defects Ni_{def} and carbon defects C_{def}, which further affects the conductivity of NiO_x. The nonstoichiometric nature of NiO_x films presents pronounced challenges for a complete understanding of coreactant effect on their electrical properties. In particular, Figure S3 illustrates the distinct effects of Ni_{def} and C_{def}. NiO_x films synthesized using ozone (T-Oz, P-Oz) and oxygen (P-Ox) as oxidizing agents in both thermal and plasma-enhanced modes feature p-type conductivity of 1.41×10^{-5}, 7.49×10^{-5}, and 8.44×10^{-5} S/cm for T-Oz, P-Oz, and P-Ox samples, respectively. These values are comparable to those of other organic p-type semiconductors employed in optoelectronics, such as Spiro-OMeTAD (1.23×10^{-4} S/cm).[89] High conductivity is attributed to the substantial presence of Ni^{3+}, which leads to the formation of nickel vacancies (V_{Ni}) that enhance p-type conductivity.[87,88] In these films, the low concentration of C_{def} produces a minimal impact on the sample conductivity. Conversely, when water was used as coreactant in both thermal (T-W) and plasma-enhanced (P-W) ALD modes, the resulting films were n-type, with conductivity values significantly higher for P-W (9.65×10^2 S/cm) compared to T-W (1.94 S/cm). These results are primarily attributed to the presence of carbon species inside the NiO_x films. C_{def} can act as interstitial and substitutional dopants, introducing new electronic states in the bandgap of NiO_x and thereby altering its conductivity.[90] In this context, the n-type conductivity is likely associated with the uncontrolled incorporation of C_{def} from the acac ligands during the ALD process. Among all of the films, NiO_x films grown by P-Ox and P-Oz exhibit electrical properties that are highly promising for optoelectronic applications, particularly as hole-transporting layers in planar perovskite solar cells. This conclusion comes from the low concentration of defects on the film surface, high concentration of Ni_{def} species, and high p-type conductivity, all contributing to efficient charge collection and enhanced device performance. In general, the values of resistivity, mobility, and carrier concentration are consistent with the data reported in the literature for ALD and CVD NiO_x (Table S1).

The resistivity of ALD NiO films can vary depending on specific conditions of the deposition process, such as temperature, precursor type, and postdeposition treatments. Generally, the resistivity of NiO_x films deposited in this way ranges from approximately 10^2 to 10^5 Ω·cm. Low resistivity values of about 10^2 Ω·cm may be obtained in the doped films or under a significant presence of defects or metallic nickel, which enhance electrical conductivity. Higher resistivity values ($\sim 10^5$ Ω·cm) are typical for more stoichiometric and pure NiO films with fewer defects and a higher degree of oxidation. The values obtained in this study vary in the range 1.04×10^{-3}–7.1×10^4 Ω·cm (Table S1), indicating broader variation related to the variety of defects that can be introduced into amorphous/crystalline NiO_x. The water-based syntheses (T-W and P-W) produce the lowest resistivities, which we attribute to a significant presence of defects or metallic nickel that enhance electrical conductivity. The plasma-based syntheses (P-Ox and P-Oz) lead to the resistivities more in line with the values reported in the literature and represent our best samples. They are typical of more stoichiometric, pure NiO_x films with fewer defects and a higher degree of oxidation. The P-Oz synthesis has an intermediate character associated with the defects determined by XPS. In particular, when O_3 and O_2 plasmas are used as oxidizing agents, the resulting films have better electrical characteristics, which make them promising materials for HTLs of perovskite solar cells.

3.7. Electronic Properties by UPS. As highlighted in the review by Cai and colleagues,[91] NiO_x films are viewed as a prospective for p–i–n perovskite solar cells, permitting us to achieve photovoltaic conversion efficiencies of 9.11–20.2%. We are particularly interested in evaluating our HTL films in heterostructures FTO/NiO/CsFAMAPbBrI/PCBM/Au and FTO/NiO/$CsPbIBr_2$/PCBM/Au for assessing their application prospects for hybrid and inorganic perovskite solar cells.

Our results show that the oxidizing agent, particularly plasma, influences the crystallographic, morphological, optical, and chemical properties of NiO_x films as well as their surface roughness. The electronic properties of the HTLs are equally important for optimal device functioning. The main challenges associated with NiO_x thin films include their low conductivity and inadequate band alignment with a perovskite, leading to suboptimal solar cell performance. The energy band structure of NiO_x films may not align well with that of a perovskite, leading to inefficient charge extraction and increased recombination losses. Solution of these challenges is crucial for achieving better performance and reliability of devices incorporating NiO_x films, particularly in applications such as perovskite solar cells.

We studied the following principal electronic properties of NiO_x films with UPS: the valence band maximum E_V, the work function φ, and the secondary electron cutoff energy E_{cutoff}. They define the band characteristics important for the HTL layer and its alignment with the absorber material (perovskite). The secondary electron cutoff E_{cutoff} (Figure 11) was determined by linear extrapolation. Alignment of the Fermi level E_F with the applied voltage bias of −7 eV allows for work function calculation using the equation $\varphi = h\nu - (E_{cutoff} - E_F)$. Here, $h\nu$ represents the energy of photons (21.1 eV) emitted by the He–I light source in the UPS system. Building on the work function values, the ionization energies were calculated as $E_I = \varphi + E_V$. Here, the value of E_V was determined by linear extrapolation (Figure S4).

The work function values obtained for nickel oxide films prepared with different coreactants were 3.67 eV (T-Oz), 3.75 eV (T-W), 4.05 eV (P-W), 4.59 eV (P-Oz), and 4.47 eV (P-Ox) as indicated in Table S2. These variations indicate that the coreactant can influence the electronic structure of the nickel oxide films. Figure S5 visually represents this effect on the

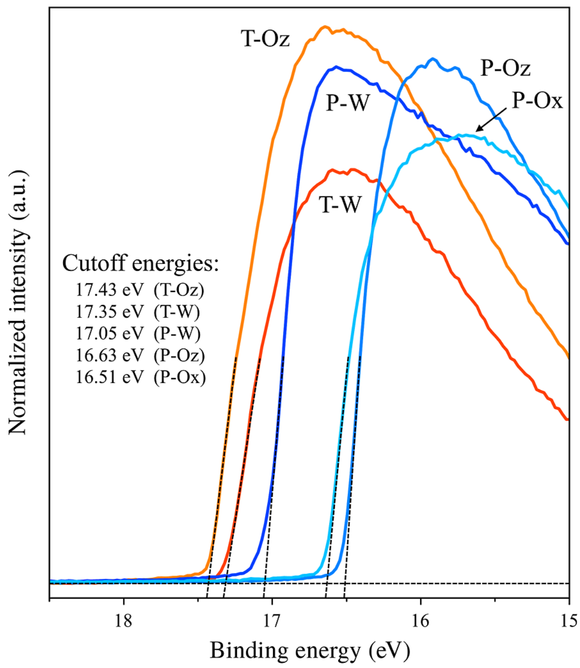

Figure 11. UPS spectra used for the determination of E_{cutoff}.

energy level diagram. Work function increases from 3.67 to 4.59 eV, indicating a significant increment of 0.92 eV. This trend is also observed in ionization energy E_I: they increase from 5.07 eV (T-W) to 5.82 eV (P-Oz)—a significant rise of 0.75 eV caused by the choice of coreactant. The films oxidized with water feature different behavior. In the P-W sample, conduction band is very close to the Fermi level E_F, which is indicative of n-type conductivity; Hall effect measurement confirms this result. In contrast, the T-W sample suggests p-type conductivity based on the band alignment. This discrepancy with electrical measurements may be attributed to nonuniformity and nonstoichiometry of the T-W sample, as evidenced by the XPS data and electrical characterization. The ozone-assisted deposition (T-Oz and P-Oz) is favorable for the NiO_x films. However, we were unable to achieve a sufficiently high hole mobility in p-type NiO_x. The P-Ox sample has its valence band E_V closer to E_F, which favors hole transport and has the potential of enhancing conductivity, which is consistent with Hall effect measurements. Therefore, the electronic structure of nickel oxide can be fine-tuned by the proper choice of oxidizing agent, as was shown by UPS results, where both φ and E_V shifted by approximately 1 eV.

For optoelectronic applications of NiO films, high ionization energy is desirable, ideally ∼5.4 eV. This high E_I promotes efficient hole extraction in p−n junctions. In our study, we explore two possible band alignments between NiO_x films and CsFAMAPbBrI (a commonly used perovskite with E_I = 5.71 eV), assuming a p−n heterojunction configuration (Figure 12) that allows for two hypothetical scenarios: a favorable alignment (Figure 12b) and unfavorable alignment (Figure 12c).

The majority of obtained NiO_x films exhibit good band alignment with CsFAMAPbBrI. Notably, the P-Ox sample stands out with the largest potential difference between its E_V and the valence band of CsFAMAPbBrI. This suggests, theoretically, that larger E_V difference may facilitate hole extraction from the perovskite. The potential difference between the perovskite and T-W, P-W, and P-Oz NiO_x films remains constant and lower than that shown by the P-Ox sample, making the latter most promising for photovoltaics applications (Figure 12b). The T-Oz sample is the most unfavorable (Figure 12c) because E_V of NiO_x is lower than that of the absorber material. Additional studies are required for the fine-tuning of these band alignments, which will eventually permit experimental validation of the proposed solar cell structures.

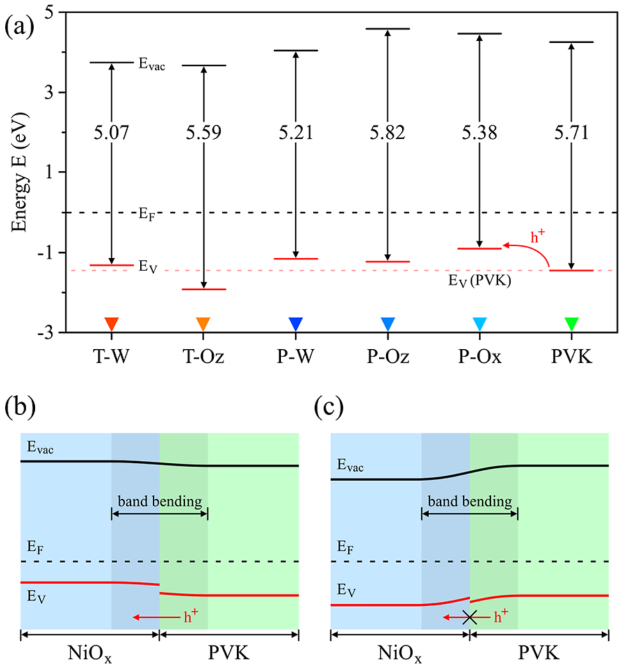

Figure 12. (a) Band alignment of NiO_x films with CsFAMAPbBrI. (b) Favorable and (c) unfavorable band alignment for the heterojunction NiO_x/CsFAMAPbBrI perovskite.

4. CONCLUSIONS

Low deposition temperature required by the $Ni(acac)_2$ precursor is one of the main obstacles for the successful growth of nickel oxide with ALD techniques. The problem consists of negligibly small reactivity of the precursor with oxygen sources (H_2O, O_3, and O_2) that are usually employed in deposition. Here, we report on the successful synthesis of thin NiO_x films with good optoelectronic and chemical properties by using different ALD techniques and oxidizing agents. To reduce the number of control parameters, we employed a simple ALD process without any pre- or postdeposition sample treatments. When water is used as an oxidation agent in both thermal and plasma-enhanced ALD, the resulting films contain a high number of defects due to suboxidation occurring in the second half of the deposition cycle; XPS analysis confirms considerable presence of Ni and C at the sample surface, causing up to 85% of transparency loss in the visible optical region. The morphological and electrical properties of the films depend significantly on the choice of oxidation agents. The best samples in this study were produced with oxygen plasma-assisted ALD. This deposition technique features high GPC (0.07 nm/cycle), short per-cycle time (12 s/cycle), and reduced carbon concentration at the sample surface (8 at. %). The use of oxygen plasma leads to the formation of water molecules, producing many OH^- groups that interchange with chemisorbed Ni(acac), making a chemical synergy with the adsorbed O^-. This mechanism is not possible with H_2O or O_3 used as the oxidizing agents. The resulting film is slightly nonstoichiometric (Ni/O ratio 0.94); it features p-type conductivity, high optical transparency (85%), good carrier concentration (8.82×10^{13} cm^{-3}), and common mobility (5.98 $cm^2/V{\cdot}s$). According to the ultraviolet photoelectron spectroscopy, the electronic properties of NiO_x (work function and valence band maximum) can be adjusted by the type of oxidation agent and ALD variant used, permitting achievement of a difference of ∼1 eV between TALD and PALD synthesis methods. Our findings indicate that PALD synthesis achieves far better energy band alignment of NiO_x with the CsFAMAPbBrI perovskite, which is promising for solar cell applications.

■ ASSOCIATED CONTENT

Supporting Information

The Supporting Information is available free of charge at https://pubs.acs.org/doi/10.1021/acsomega.4c06606.

AFM of NiO_x films; ellipsometry data (Ψ, Δ, n, and k) for the P-Ox sample; conductivity and Hall coefficient of NiO_x films; main electrical properties of NiO_x films compared to the literature data; UPS spectra used for the calculation of valence band maximum; main physical parameters of NiO_x films extracted from UPS measurements; and band alignment of NiO_x samples and the perovskite absorber CsFAMAPbBrI (PDF)

■ AUTHOR INFORMATION

Corresponding Author

Eduardo Martínez-Guerra − *Centro de Investigación en Materiales Avanzados, S.C. (CIMAV Subsede Monterrey), 66628 Apodaca, Nuevo León, Mexico;* orcid.org/0000-0002-2308-1259; Email: eduardo.martinez@cimav.edu.mx

Authors

Mario Alberto Hidrogo-Rico − *Centro de Investigación en Materiales Avanzados, S.C. (CIMAV Subsede Monterrey), 66628 Apodaca, Nuevo León, Mexico*

Nicola Nedev − *Instituto de Ingeniería, Universidad Autónoma de Baja California, 21280 Mexicali, Baja California, Mexico*

Paul Horley − *Centro de Investigación en Materiales Avanzados, S.C. (CIMAV Subsede Monterrey), 66628 Apodaca, Nuevo León, Mexico*

María Isabel Mendívil − *Centro de Investigación en Materiales Avanzados, S.C. (CIMAV Subsede Monterrey), 66628 Apodaca, Nuevo León, Mexico*

Jhonathan Castillo-Saenz − *Instituto de Ingeniería, Universidad Autónoma de Baja California, 21280 Mexicali, Baja California, Mexico;* orcid.org/0000-0003-0877-2198

Edgar Martínez-Guerra − *Facultad de Ciencias Físico-Matemáticas, Universidad Autónoma de Nuevo León, 65480 San Nicolás de los Garza, Nuevo León, Mexico*

Emilio J. Juarez-Perez − *Nanostructured Films & Particles Research Group (NFP). Instituto de Nanociencia y Materiales de Aragón (INMA), CSIC Universidad de Zaragoza, 50009 Zaragoza, Spain*

Francisco Servando Aguirre-Tostado − *Centro de Investigación en Materiales Avanzados, S.C. (CIMAV Subsede Monterrey), 66628 Apodaca, Nuevo León, Mexico;* orcid.org/0000-0002-8721-0179

Arturo Susarrey-Arce − *Mesoscale Chemical Systems, MESA+ Institute, University of Twente, 7522 NB Enschede, The Netherlands;* orcid.org/0000-0003-2572-223X

Complete contact information is available at: https://pubs.acs.org/10.1021/acsomega.4c06606

Notes

The authors declare no competing financial interest.

■ ACKNOWLEDGMENTS

This work was partially supported by the bilateral project CONAHCYT-AFOSR cc0015-2016-05-279915 “Single crystal and thin film hybrid perovskite materials for optoelectronic applications”. We appreciate the high-quality measurements and technical assistance of L.G. Silva-Vidaurri, A. Arizpe-Zapata, A. Concha-Balderama, O.E. Vega-Becerra, and L.M. Bautista-Carrillo.

■ REFERENCES

(1) Conell, R. S.; Corrigan, D. A.; Powell, B. R. The electrochromic properties of sputtered nickel oxide films. *Sol. Energy Mater. Sol. Cells* **1992**, *25*, 301−313.

(2) Soo Kim, D.; Chul Lee, H. Nickel vacancy behavior in the electrical conductance of nonstoichiometric nickel oxide film. *J. Appl. Phys.* **2012**, *112*, 034504.

(3) Kaya, D.; Aydınoğlu, H. S.; Şenadım Tüzemen, E.; Ekicibil, A. Investigation of optical, electronic, and magnetic properties of p-type NiO thin film on different substrates. *Thin Solid Films* **2021**, *732*, 138800.

(4) Patil, P.; Kadam, L. Preparation and characterization of spray pyrolyzed nickel oxide (NiO) thin films. *Appl. Surf. Sci.* **2002**, *199*, 211−221.

(5) Dubey, P.; Kaurav, N.; Devan, R. S.; Okram, G. S.; Kuo, Y. K. The effect of stoichiometry on the structural, thermal and electronic properties of thermally decomposed nickel oxide. *RSC Adv.* **2018**, *8*, 5882−5890.

(6) Nattestad, A.; Mozer, A. J.; Fischer, M. K. R.; Cheng, Y.-B.; Mishra, A.; Bäuerle, P.; Bach, U. Highly efficient photocathodes for dye-sensitized tandem solar cells. *Nat. Mater.* **2010**, *9*, 31−35.

(7) Nachman, M.; Cojocaru, L. N.; Rîbco, L. V. Electrical properties of non-stoichiometric nickel oxide. *Phys. Status Solidi* **1965**, *8*, 773−783.

(8) Sugiyama, I.; Shibata, N.; Wang, Z.; Kobayashi, S.; Yamamoto, T.; Ikuhara, Y. Ferromagnetic dislocations in antiferromagnetic NiO. *Nat. Nanotechnol.* **2013**, *8*, 266−270.

(9) Sato, H.; Minami, T.; Takata, S.; Yamada, T. Transparent conducting p-type NiO thin films prepared by magnetron sputtering. *Thin Solid Films* **1993**, *236*, 27−31.

(10) Kitao, M.; Izawa, K.; Urabe, K.; Komatsu, T.; Kuwano, S.; Yamada, S. Preparation and electrochromic properties of RF-Sputtered NiO_x films prepared in $Ar/O_2/H_2$ atmosphere. *Jpn. J. Appl. Phys.* **1994**, *33*, 6656−6662.

(11) Yoshimura, K.; Miki, T.; Iwama, S.; Sakae Tanemura, S. T. Niobium oxide electrochromic thin films prepared by reactive DC magnetron sputtering. *Jpn. J. Appl. Phys.* **1995**, *34*, L1293.

(12) Kumagai, H.; Matsumoto, M.; Toyoda, K.; Obara, M. Preparation and characteristics of nickel oxide thin film by controlled growth with sequential surface chemical reactions. *J. Mater. Sci. Lett.* **1996**, *15*, 1081−1083.

(13) Sajid, S.; Elseman, A. M.; Huang, H.; Ji, J.; Dou, S.; Jiang, H.; Liu, X.; Wei, D.; Cui, P.; Li, M. Breakthroughs in NiO_x-HTMs towards stable, low-cost and efficient perovskite solar cells. *Nano Energy* **2018**, *51*, 408−424.

(14) Napari, M.; Huq, T. N.; Hoye, R. L. Z.; MacManus-Driscoll, J. L. Nickel oxide thin films grown by chemical deposition techniques: Potential and challenges in next-generation rigid and flexible device applications. *InfoMat* **2021**, *3*, 536−576.

(15) Misra, P.; Sahu, V. K.; Ajimsha, R. S.; Das, A. K.; Singh, B. Studies on resistive switching times in NiO thin films grown by pulsed laser deposition. *J. Phys. D Appl. Phys.* **2017**, *50*, 415106.

(16) Reddy, A. M.; Reddy, A. S.; Lee, K.-S.; Reddy, P. S. Growth and characterization of NiO thin films prepared by dc reactive magnetron sputtering. *Solid State Sci.* **2011**, *13*, 314−320.

(17) Pereira, S.; Gonçalves, A.; Correia, N.; Pinto, J.; Pereira, L.; Martins, R.; Fortunato, E. Electrochromic behavior of NiO thin films deposited by e-beam evaporation at room temperature. *Sol. Energy Mater. Sol. Cells* **2014**, *120*, 109−115.

(18) Jlassi, M.; Sta, I.; Hajji, M.; Ezzaouia, H. NiO thin films synthesized by sol-gel: Potentiality for the realization of antireflection layer for silicon based solar cell applications. *Surf. Interfaces* **2017**, *6*, 218−222.

(19) Ivanova, T.; Harizanova, A.; Shipochka, M.; Vitanov, P. Nickel oxide films deposited by sol-gel method: Effect of annealing temperature on structural, optical, and electrical properties. *Materials* **2022**, *15*, 1742.

(20) Roffi, T. M.; Nozaki, S.; Uchida, K. Growth mechanism of single-crystalline NiO thin films grown by metal organic chemical vapor deposition. *J. Cryst. Growth* **2016**, *451*, 57−64.

(21) Ismail, R. A.; Ghafori, S.; Kadhim, G. A. Preparation and characterization of nanostructured nickel oxide thin films by spray pyrolysis. *Appl. Nanosci.* **2013**, *3*, 509−514.

(22) Koushik, D.; Jošt, M.; Dučinskas, A.; Burgess, C.; Zardetto, V.; Weijtens, C.; Verheijen, M. A.; Kessels, W. M. M.; Albrecht, S.; Creatore, M. Plasma-assisted atomic layer deposition of nickel oxide as hole transport layer for hybrid perovskite solar cells. *J. Mater. Chem. C* **2019**, *7*, 12532−12543.

(23) Hufnagel, A. G.; Henß, A. K.; Hoffmann, R.; Zeman, O. E. O.; Häringer, S.; Fattakhova-Rohlfing, D.; Bein, T. Electron-blocking and oxygen evolution catalyst layers by plasma-enhanced atomic layer deposition of nickel oxide. *Adv. Mater. Interfaces* **2018**, *5*, 1701531.

(24) Ji, S. H.; Jang, W. S.; Son, J. W.; Kim, D. H. Characteristics of NiO films prepared by atomic layer deposition using bis-(ethylcyclopentadienyl)-Ni and O_2 plasma. *Korean J. Chem. Eng.* **2018**, *35*, 2474−2479.

(25) Koshtyal, Y.; Nazarov, D.; Ezhov, I.; Mitrofanov, I.; Kim, A.; Rymyantsev, A.; Lyutakov, O.; Popovich, A.; Maximov, M. Atomic layer deposition of NiO to produce active material for thin-film lithium-ion batteries. *Coatings* **2019**, *9*, 301.

(26) Phung, N.; van Helvoirt, C.; Beyer, W.; Anker, J.; Naber, R. C. G.; Renes, M.; Kessels, W. M. M.; Geerligs, L. J.; Creatore, M.; Macco, B. Effective hydrogenation of poly-Si passivating contacts by atomic-layer-deposited nickel oxide. *IEEE. J Photovoltaics* **2022**, *12*, 1377.

(27) Zardetto, V.; Williams, B. L.; Perrotta, A.; Di Giacomo, F.; Verheijen, M. A.; Andriessen, R.; Kessels, W. M. M.; Creatore, M. Atomic layer deposition for perovskite solar cells: research status, opportunities and challenges. *Sustain. Energy Fuels* **2017**, *1*, 30−55.

(28) Napari, M.; Huq, T. N.; Maity, T.; Gomersall, D.; Niang, K. M.; Barthel, A.; Thompson, J. E.; Kinnunen, S.; Arstila, K.; Sajavaara, T.; Hoye, R. L. Z.; Flewitt, A. J.; MacManus-Driscoll, J. L. Antiferromagnetism and p-type conductivity of nonstoichiometric nickel oxide thin films. *InfoMat* **2020**, *2*, 769−774.

(29) Profijt, H. B.; Potts, S. E.; van de Sanden, M. C. M.; Kessels, W. M. M. Plasma-assisted atomic layer deposition: Basics, opportunities, and challenges. *J. Vac. Sci. Technol., A* **2011**, *29*, 050801.

(30) Garcia-Alonso, D.; Potts, S. E.; Van Helvoirt, C. A. A.; Verheijen, M. A.; Kessels, W. M. M. Atomic layer deposition of B-doped ZnO using triisopropyl borate as the boron precursor and comparison with Al-doped ZnO. *J. Mater. Chem. C* **2015**, *3*, 3095−3107.

(31) Chae, J.; Park, H. S.; Kang, S. W. Atomic layer deposition of nickel by the reduction of preformed nickel oxide. *Electrochem. Solid-State Lett.* **2002**, *5*, C64.

(32) Kim, D. H.; Sim, J. K.; Lee, J.; Seo, H. O.; Jeong, M. G.; Kim, Y. D.; Kim, S. H. Carbon dioxide reforming of methane over mesoporous Ni/SiO_2. *Fuel* **2013**, *112*, 111−116.

(33) Jeong, M. G.; Kim, D. H.; Lee, S. K.; Lee, J. H.; Han, S. W.; Park, E. J.; Cychosz, K. A.; Thommes, M.; Hwang, Y. K.; Chang, J. S.; Kim, Y. D. Decoration of the internal structure of mesoporous chromium terephthalate MIL-101 with NiO using atomic layer deposition. *Microporous Mesoporous Mater.* **2016**, *221*, 101−107.

(34) Wang, G.; Gao, Z.; Wan, G.; Lin, S.; Yang, P.; Qin, Y. High densities of magnetic nanoparticles supported on graphene fabricated by atomic layer deposition and their use as efficient synergistic microwave absorbers. *Nano Res.* **2014**, *7*, 704−716.

(35) Lu, H. L.; Scarel, G.; Wiemer, C.; Perego, M.; Spiga, S.; Fanciulli, M.; Pavia, G. Atomic layer deposition of NiO films on Si(100) using cyclopentadienyl-type compounds and ozone as precursors. *J. Electrochem. Soc.* **2008**, *155*, H807.

(36) Wang, G.; Peng, X.; Yu, L.; Wan, G.; Lin, S.; Qin, Y. Enhanced microwave absorption of ZnO coated with Ni nanoparticles produced by atomic layer deposition. *J. Mater. Chem. A* **2015**, *3*, 2734−2740.

(37) Gao, Z.; Dong, M.; Wang, G.; Sheng, P.; Wu, Z.; Yang, H.; Zhang, B.; Wang, G.; Wang, J.; Qin, Y. Multiply confined nickel nanocatalysts produced by atomic layer deposition for hydrogenation reactions. *Angew. Chem.* **2015**, *127*, 9134−9138.

(38) Alburquenque, D.; del Canto, M.; Arenas, C.; Tejo, F.; Pereira, A.; Escrig, J. Dewetting of Ni thin films obtained by atomic layer deposition due to the thermal reduction process: Variation of the thicknesses. *Thin Solid Films* **2017**, *638*, 114−118.

(39) Zhang, J.; Chen, C.; Yan, W.; Duan, F.; Zhang, B.; Gao, Z.; Qin, Y. Ni nanoparticles supported on CNTs with excellent activity produced by atomic layer deposition for hydrogen generation from the hydrolysis of ammonia borane. *Catal. Sci. Technol.* **2016**, *6*, 2112−2119.

(40) Zhang, R.; Wei, H.; Si, W.; Ou, G.; Zhao, C.; Song, M.; Zhang, C.; Wu, H. Enhanced electrocatalytic activity for water splitting on NiO/Ni/carbon fiber paper. *Mater.* **2017**, *10*, 15.

(41) Yang, G.; Xiang, H.; Rauf, M.; Mi, H.; Ren, X.; Zhang, P.; Li, Y. Plasma enhanced atomic-layer-deposited nickel oxide on Co_3O_4 arrays as highly active electrocatalyst for oxygen evolution reaction. *J. Power Sources* **2021**, *481*, 228925.

(42) Holden, K. E. K.; Dezelah, C. L.; Conley, J. F. Atomic layer deposition of transparent p-type semiconducting nickel oxide using $Ni(tBu_2DAD)_2$ and ozone. *ACS Appl. Mater. Interfaces* **2019**, *11*, 30437−30445.

(43) Zhang, Y.; Du, L.; Liu, X.; Ding, Y. A high growth rate atomic layer deposition process for nickel oxide film preparation using a combination of nickel (II) diketonate−diamine and ozone. *Appl. Surf. Sci.* **2019**, *481*, 138−143.

(44) Lindblad, M.; Lindfors, L. P.; Suntola, T. Preparation of Ni/Al_2O_3 catalysts from vapor phase by atomic layer epitaxy. *Catal. Lett.* **1994**, *27*, 323−336.

(45) Jacobs, J. P.; Lindfors, L. P.; Reintjes, J. G. H.; Jylhä, O.; Brongersma, H. H. The growth mechanism of nickel in the preparation of Ni/Al_2O_3 catalysts studied by LEIS, XPS and catalytic activity. *Catal. Lett.* **1994**, *25*, 315−324.

(46) Utriainen, M.; Kröger-Laukkanen, M.; Johansson, L. S.; Niinistö, L. Studies of metallic thin film growth in an atomic layer epitaxy reactor using $M(acac)_2$ (M = Ni, Cu, Pt) precursors. *Appl. Surf. Sci.* **2000**, *157*, 151−158.

(47) Huang, H. W.; Chang, W. C.; Lin, S. J.; Chueh, Y. L. Growth of controllable ZnO film by atomic layer deposition technique via inductively coupled plasma treatment. *J. Appl. Phys.* **2012**, *112*, 124102.

(48) Shi, Z.; Walker, A. V. Room temperature atomic layer-like deposition of ZnO on functionalized self-assembled monolayers. *J. Phys. Chem. C* **2015**, *119*, 1091−1100.

(49) Lee, W.; Jeon, W.; An, C. H.; Chung, M. J.; Kim, H. J.; Eom, T.; George, S. M.; Park, B. K.; Han, J. H.; Kim, C. G.; Chung, T. M.; Lee, S. W.; Hwang, C. S. Improved initial growth behavior of SrO and $SrTiO_3$ films grown by atomic layer deposition using $\{Sr(demamp)(tmhd)\}_2$ as Sr-precursor. *Chem. Mater.* **2015**, *27*, 3881−3891.

(50) Minjauw, M. M.; Solano, E.; Sree, S. P.; Asapu, R.; Van Daele, M.; Ramachandran, R. K.; Heremans, G.; Verbruggen, S. W.;

Lenaerts, S.; Martens, J. A.; Detavernier, C.; Dendooven, J. Plasma-enhanced atomic layer deposition of silver using Ag(fod)(PEt_3) and NH_3-plasma. *Chem. Mater.* **2017**, *29*, 7114−7121.

(51) Bartholazzi, G.; Shehata, M. M.; Macdonald, D. H.; Black, L. E. Atomic layer deposition of Cu_2O using copper acetylacetonate. *J. Vac. Sci. Technol., A* **2023**, *41*, 022402.

(52) XPS OASIS download. https://xpsoasis.org/download (accessed December 13, 2022).

(53) Herrera-Gomez, A.; Bravo-Sanchez, M.; Ceballos-Sanchez, O.; Vazquez-Lepe, M. O. Practical methods for background subtraction in photoemission spectra. *Surf. Interface Anal.* **2014**, *46*, 897−905.

(54) Nalwa, H. S. *Handbook of thin film materials*; Academic Press: San Diego, 2002

(55) Bratvold, J. E.; Fjellvåg, H.; Nilsen, O. Atomic layer deposition of oriented nickel titanate ($NiTiO_3$). *Appl. Surf. Sci.* **2014**, *311*, 478−483.

(56) Utriainen, M.; Kröger-Laukkanen, M.; Niinistö, L. Studies of NiO thin film formation by atomic layer epitaxy. *Mater. Sci. Eng., B* **1998**, *54*, 98−103.

(57) Castillo-Saenz, J.; Nedev, N.; Valdez-Salas, B.; Curiel-Alvarez, M.; Mendivil-Palma, M. I.; Hernandez-Como, N.; Martinez-Puente, M.; Mateos, D.; Perez-Landeros, O.; Martinez-Guerra, E. Properties of Al_2O_3 thin films grown by PE-ALD at low temperature using H_2O and O_2 plasma oxidants. *Coatings* **2021**, *11*, 1266.

(58) Martínez-Puente, M. A.; Tirado, J.; Jaramillo, F.; Garza-Hernández, R.; Horley, P.; Silva Vidaurri, L. G.; Aguirre-Tostado, F. S.; Martínez-Guerra, E. Unintentional hydrogen incorporation into the SnO_2 electron transport layer by ALD and its effect on the electronic band structure. *ACS Appl. Energy Mater.* **2021**, *4*, 10896−10908.

(59) Ramírez-Esquivel, O. Y.; Mazón-Montijo, D. A.; Cabrera-German, D.; Martínez-Guerra, E.; Montiel-González, Z. Atomic layer deposition supercycle approach applied to the Al-doping of nearly saturated ZnO surfaces. *Ceram. Int.* **2021**, *47*, 7126−7134.

(60) Hu, X.; Schuster, J.; Schulz, S. E.; Gessner, T. Surface chemistry of copper metal and copper oxide atomic layer deposition from copper (ii) acetylacetonate: a combined first-principles and reactive molecular dynamics study. *Phys. Chem. Chem. Phys.* **2015**, *17*, 26892−26902.

(61) Sarr, M.; Bahlawane, N.; Arl, D.; Dossot, M.; McRae, E.; Lenoble, D. Tailoring the properties of atomic layer deposited nickel and nickel carbide thin films via chain-length control of the alcohol reducing agents. *J. Phys. Chem. C* **2014**, *118*, 23385−23392.

(62) Antony Premkumar, P.; Toeller, M.; Adelmann, C.; Meersschaut, J.; Franquet, A.; Richard, O.; Tielens, H.; Brijs, B.; Moussa, A.; Conard, T.; Bender, H.; Schaekers, M.; Kittl, J. A.; Jurczak, M.; van Elshocht, S. NiO thin films synthesized by atomic layer deposition using $Ni(dmamb)_2$ and ozone as precursors. *Chem. Vap. Depos.* **2012**, *18*, 61−69.

(63) Hellenbrandt, M. The inorganic crystal structure database (ICSD). *Present and Future* **2004**, *10*, 17−22.

(64) Boris, D. R.; Wheeler, V. D.; Nepal, N.; Qadri, S. B.; Walton, S. G.; Eddy, C. C. R. The role of plasma in plasma-enhanced atomic layer deposition of crystalline films. *J. Vac. Sci. Technol., A* **2020**, *38*, 040801.

(65) Weiss, T.; Zielasek, V.; Bäumer, M. Influence of water on chemical vapor deposition of Ni and Co thin films from ethanol solutions of acetylacetonate precursors. *Sci. Reports* **2016**, *5*, 18194.

(66) Ylilammi, M. Monolayer thickness in atomic layer deposition. *Thin Solid Films* **1996**, *279*, 124−130.

(67) Martínez-Gil, M.; Pintor-Monroy, M. I.; Cota-Leal, M.; Cabrera-German, D.; Garzon-Fontecha, A.; Quevedo-López, M. A.; Sotelo-Lerma, M. Influence of annealing temperature on nickel oxide thin films grown by chemical bath deposition. *Mater. Sci. Semicond. Process.* **2017**, *72*, 37−45.

(68) Xie, L.-Y.; Xiao, D.-Q.; Pei, J.-X.; Huo, J.; Wu, X.; Liu, W.-J.; Ding, S.-J. Growth, physical and electrical characterization of nickel oxide thin films prepared by plasma-enhanced atomic layer deposition using nickelocene and oxygen precursors. *Mater. Res. Express* **2020**, *7*, 046401.

(69) Grosvenor, A. P.; Biesinger, M. C.; Smart, R. S. C.; McIntyre, N. S. New interpretations of XPS spectra of nickel metal and oxides. *Surf. Sci.* **2006**, *600*, 1771−1779.

(70) van Veenendaal, M. A.; Sawatzky, G. A. Nonlocal screening effects in 2p X-ray photoemission spectroscopy core-level line shapes of transition metal compounds. *Phys. Rev. Lett.* **1993**, *70*, 2459−2462.

(71) Mossanek, R. J. O.; Preda, I.; Abbate, M.; Rubio-Zuazo, J.; Castro, G. R.; Vollmer, A.; Gutiérrez, A.; Soriano, L. Investigation of surface and non-local screening effects in the Ni 2p core level photoemission spectra of NiO. *Chem. Phys. Lett.* **2011**, *501*, 437−441.

(72) Tomellini, M. A comment on "Final states after Ni 2p photoemission in NiO". *J. Electron Spectrosc. Relat. Phenom.* **1992**, *58*, 75−78.

(73) Carley, A. F.; Jackson, S. D.; O'Shea, J. N.; Roberts, M. W. The formation and characterisation of Ni^{3+} − an X-ray photoelectron spectroscopic investigation of potassium-doped Ni(110)−O. *Surf. Sci.* **1999**, *440*, L868−L874.

(74) Soriano, L.; Preda, I.; Gutiérrez, A.; Palacín, S.; Abbate, M.; Vollmer, A. Surface effects in the Ni 2p X-ray photoemission spectra of NiO. *Phys. Rev. B* **2007**, *75*, 233417.

(75) Alders, D.; Sawatzky, G.; Voogt, F.; Hibma, T. Nonlocal screening effects in 2p X-ray photoemission spectroscopy of NiO (100). *Phys. Rev. B* **1996**, *54*, 7716.

(76) Biesinger, M. C.; Payne, B. P.; Lau, L. W. M.; Gerson, A.; Smart, R. St.C. X-ray photoelectron spectroscopic chemical state quantification of mixed nickel metal, oxide and hydroxide systems. *Surf. Interface Anal.* **2009**, *41*, 324−332.

(77) Wang, K.-C.; Shen, P.-S.; Li, M.-H.; Chen, S.; Lin, M.-W.; Chen, P.; Guo, T.-F. Low-temperature sputtered nickel oxide compact thin film as effective electron blocking layer for mesoscopic NiO/$CH_3NH_3PbI_3$ perovskite heterojunction solar cells. *ACS Appl. Mater. Interfaces* **2014**, *6*, 11851−11858.

(78) Kwon, U.; Kim, B.-G.; Nguyen, D. C.; Park, J.-H.; Ha, N. Y.; Kim, S.-J.; Ko, S. H.; Lee, S.; Lee, D.; Park, H. J. Solution-processible crystalline NiO nanoparticles for high-performance planar perovskite photovoltaic cells. *Sci. Rep.* **2016**, *6*, 30759.

(79) Qiu, Z.; Gong, H.; Zheng, G.; Yuan, S.; Zhang, H.; Zhu, X.; Zhou, H.; Cao, B. Enhanced physical properties of pulsed laser deposited NiO films via annealing and lithium doping for improving perovskite solar cell efficiency. *J. Mater. Chem. C* **2017**, *5*, 7084−7094.

(80) Gnanasekaran, L.; Manoj, D.; Rajendran, S.; Gracia, F.; Jalil, A. A.; Chen, W.-H.; Soto-Moscoso, M.; Gracia-Pinilla, M. A. Mesoporous NiO/Ni_2O_3 nanoflowers for favorable visible light photocatalytic degradation of 4-chlorphenol. *Environ. Res.* **2023**, *236*, 116790.

(81) Hagelin-Weaver, H. A. E.; Weaver, J. F.; Hoflund, G. B.; Salaita, G. N. Electron energy loss spectroscopic investigation of Ni metal and NiO before and after surface reduction by Ar^+ bombardment. *J. Electron Spectrosc. Relat. Phenom.* **2004**, *134*, 139−171.

(82) Gupta, R. P.; Sen, S. K. Calculation of multiplet structure of core p-vacancy levels. *Phys. Rev. B* **1974**, *10*, 71−77.

(83) Gupta, R. P.; Sen, S. K. Calculation of multiplet structure of core p-vacancy levels II. *Phys. Rev. B* **1975**, *12*, 15−19.

(84) Hagelin-Weaver, H. A. E.; Weaver, J. F.; Hoflund, G. B.; Salaita, G. N. Electron energy loss spectroscopy study of nickel, chromium and nickel-chromium alloy. *J. Alloys Compd.* **2005**, *389*, 34−41.

(85) Lu, H. L.; Scarel, G.; Alia, M.; Fanciulli, M.; Ding, S. J.; Zhang, D. W. Spectroscopic ellipsometry study of thin NiO films grown on Si (100) by atomic layer deposition. *Appl. Phys. Lett.* **2008**, *92*, 222907.

(86) López-Beltrán, A. M.; Mendoza-Galván, A. The oxidation kinetics of nickel thin films studied by spectroscopic ellipsometry. *Thin Solid Films* **2006**, *503*, 40−44.

(87) Wang, K. C.; Shen, P. S.; Li, M. H.; Chen, S.; Lin, M. W.; Chen, P.; Guo, T. F. Low-temperature sputtered nickel oxide compact thin film as effective electron blocking layer for mesoscopic NiO/$CH_3NH_3PbI_3$ perovskite heterojunction solar cells. *ACS Appl. Mater. Interfaces* **2014**, *6*, 11851−11858.

(88) Qiu, Z.; Gong, H.; Zheng, G.; Yuan, S.; Zhang, H.; Zhu, X.; Zhou, H.; Cao, B. Enhanced physical properties of pulsed laser deposited NiO films via annealing and lithium doping for improving perovskite solar cell efficiency. *J. Mater. Chem. C* **2017**, *5*, 7084−7094.

(89) Tabor, D. P.; Chiykowski, V. A.; Friederich, P.; Cao, Y.; Dvorak, D. J.; Berlinguette, C. P.; Aspuru-Guzik, A. Design rules for high mobility xanthene-based hole transport materials. *Chem. Sci.* **2019**, *10*, 8360−8366.

(90) Cantrell, S. R.; Welch, E.; Scolfaro, L. M.; Geerts, W. J. Optoelectronic properties of carbon doped NiO. *J. Phys. Chem. Solids* **2023**, *174*, 111110.

(91) Cai, X.; Hu, T.; Hou, H.; Zhu, P.; Liu, R.; Peng, J.; Luo, W.; Yu, H. A review for nickel oxide hole transport layer and its application in halide perovskite solar cells. *Mater. Today Sustain.* **2023**, *23*, 100438.